An evaluation of plastic flow stress models for the simulation of high-temperature and high-strain-rate deformation of metals

Biswajit Banerjee [1]

Department of Mechanical Engineering, University of Utah, 50 S Central Campus Dr.,
MEB 2110, Salt Lake City, UT 84112, USA

Abstract

Phenomenological plastic flow stress models are used extensively in the simulation of large deformations of metals at high strain-rates and high temperatures. Several such models exist and it is difficult to determine the applicability of any single model to the particular problem at hand. Ideally, the models are based on the underlying (subgrid) physics and therefore do not need to be recalibrated for every regime of application. In this work we compare the Johnson-Cook, Steinberg-Cochran-Guinan-Lund, Zerilli-Armstrong, Mechanical Threshold Stress, and Preston-Tonks-Wallace plasticity models. We use OFHC copper as the comparison material because it is well characterized. First, we determine parameters for the specific heat model, the equation of state, shear modulus models, and melt temperature models. These models are evaluated and their range of applicability is identified. We then compare the flow stresses predicted by the five flow stress models with experimental data for annealed OFHC copper and quantify modeling errors. Next, Taylor impact tests are simulated, comparison metrics are identified, and the flow stress models are evaluated on the basis of these metrics. The material point method is used for these computations. We observe that the all the models are quite accurate at low temperatures and any of these models could be used in simulations. However, at high temperatures and under high-strain-rate conditions, their accuracy can vary significantly.

Key words: Dynamics, thermomechanical processes, constitutive behavior, elastic-viscoplastic material, finite strain.

---

[1] Phone: 1-801-585-5239, Fax: 1-801-585-0039, Email: banerjee@eng.utah.edu

Preprint submitted to Elsevier Science *17 December 2005*

1 Introduction

The Uintah computational framework (de St. Germain et al. (2000)) was developed to provide tools for the simulation of multi-physics problems such as the interaction of fires with containers, the explosive deformation and fragmentation of metal containers, impact and penetration of materials, dynamics deformation of air-filled metallic foams, and other such situations. Most of these situations involve high strain-rates. In some cases there is the additional complication of high temperatures. This work arose out of the need to validate the Uintah code and to quantify modeling errors in the subgrid scale physics models.

Plastic flow stress models and the associated specific heat, shear modulus, melting temperature, and equation of state models are subgrid scale models of complex deformation phenomena. It is unreasonable to expect that any one model will be able to capture all the subgrid scale physics under all possible conditions. We therefore evaluate a number of models which are best suited to the regime of interest to us. This regime consists of strain-rates between 10^3 /s and 10^6 /s and temperatures between 230 K and 800 K. We have observed that the combined effect of high temperature and high strain-rates has been glossed over in most other similar works (for example Zerilli and Armstrong (1987); Johnson and Holmquist (1988); Zocher et al. (2000)). Hence we examine the temperature dependence of plastic deformation at high strain-rates in some detail in this paper.

In this paper, we attempt to quantify the modeling errors that we get when we model large-deformation plasticity (at high strain-rates and high temperatures) with five recently developed models. These models are the Johnson-Cook model (Johnson and Cook (1983)), the Steinberg-Cochran-Guinan-Lund model (Steinberg et al. (1980); Steinberg and Lund (1989)), the Zerilli-Armstrong model (Zerilli and Armstrong (1987)), the Mechanical Threshold Stress model (Follansbee and Kocks (1988)), and the Preston-Tonks-Wallace model (Preston et al. (2003)). We also evaluate the associated shear modulus models of Varshni (1970), Steinberg et al. (1980), and Nadal and Le Poac (2003). The melting temperature models of Steinberg et al. (1980) and Burakovsky et al. (2000a) are also examined. A temperature-dependent specific heat relation is used to compute specific heats and a form of the Mie-Grüneisen equation of state that assumes a linear slope for the Hugoniot curve are also evaluated. We suggest that the model that is most appropriate for a given set of conditions can be chosen with greater confidence once the modeling errors are quantified,

The most common approach for determining modeling error is the comparison of predicted uniaxial stress-strain curves with experimental data. For high strain-rate conditions, flyer plate impact tests provide further one-dimensional data that can be used to evaluate plasticity models. Taylor impact tests (Taylor (1948)) can be use to obtain two-dimensional estimates of modeling errors. We restrict ourselves to comparing uniaxial tests and Taylor impact tests in this paper; primarily because high-temperature flyer plate impact experimental data are not readily available in the literature. We simulate uniaxial tests and Taylor impact tests with the Material Point Method (Sulsky et al. (1994, 1995)). The model parameters that we use in these simulations are, for the most part, the values that are available in the literature. We do not recalibrate the models to fit the experimental data that we use for our comparisons. For simplicity, we use annealed OFHC copper as the material for which we evaluate all the models because this material is well-characterized. A similar exercise for various tempers of 4340 steel can be found elsewhere (Banerjee (2005a)).

Most comparisons between experimental data and simulations involve the visual estimation of errors. For example, two stress-strain curves or two Taylor specimen profiles are overlaid on a graph and the viewer estimates the difference between the two. We extend this approach by providing quantitative estimates of the error and providing metrics with which such estimates can be made. The metrics are discussed and the models are evaluated on the basis of these metrics.

The organization of this paper is as follows. Section 2 discusses the specific heat model, the equation of state, the melting temperature models, and the shear modulus models. Flow stress models are discussed in Section 3 and evaluated on the basis of one-dimensional tension and shear tests. Section 4 discusses experimental data, metrics, and simulations of Taylor impact tests. Conclusions are presented in Section 5.

2 Models

In most computations involving plastic deformation, the specific heat, the shear modulus, and the melting temperature are assumed to be constant. However, the shear modulus is known to vary with temperature and pressure. The melting temperature can increase dramatically at the large pressures experienced during high strain-rate deformation. In some materials, the specific heat can also change significantly with change in temperature. If the range of temperatures and strain-rates is small then these variations can be ignored. However, if a simulation involves a change in strain-rate from quasistatic to explosive, and a change in temperature from ambient values to values that are close to the melt temperature, the temperature- and pressure-dependence of these physical properties has to be taken into consideration.

The models used in our simulations are discussed in this section. The material response is assumed to be isotropic. The stress is decomposed into a volumetric and a deviatoric part. The volumetric part of the stress is computed using the equation of state. The deviatoric part of the stress is computed using an additive decomposition of the rate of deformation into elastic and plastic parts, the von Mises yield condition, and a flow stress model. The variable shear modulus is used to update both the elastic and plastic parts of the stress and is also used by some of the flow stress models. The melting temperature model is used to determine if the material has melted locally and also feeds into one of the shear modulus models. The increase in temperature due to the dissipation of plastic work is computed using the variable specific heat model. We stress physically-based models in this work because these can usually be used in a larger range of conditions than empirical models and need less recalibration.

Copper shows significant strain hardening, strain-rate sensitivity, and temperature dependence of plastic flow behavior. The material is quite well characterized and a significant amount of experimental data are available for copper in the open literature. Hence it is invaluable for testing the accuracy of plasticity models and validating codes that simulate plasticity. In this work, we have only considered fully annealed oxygen-free high conductivity (OFHC) copper and electrolytic tough pitch (ETP) copper.

2.1 Adiabatic Heating, Specific Heat, Thermal Conductivity

A part of the plastic work done is converted into heat and used to update the temperature of a particle. The increase in temperature (ΔT) due to an increment in plastic strain ($\Delta\epsilon_p$) is given by the equation

$$\Delta T = \frac{\chi\sigma_y}{\rho C_p}\Delta\epsilon_p \tag{1}$$

where χ is the Taylor-Quinney coefficient (Taylor and Quinney (1934)), and C_p is the specific heat. The value of the Taylor-Quinney coefficient is assumed to be 0.9 in all our simulations (see Ravichandran et al. (2001) for more details on the variation of χ with strain and strain-rate). The specific heat is also used in the estimation of the change in internal energy required by the Mie-Grüneisen equation of state.

The specific heat (C_p) versus temperature (T) model used in our simulations of copper has the form shown below. The units of C_p are J/kg-K and the units of T are degrees K.

$$C_p = \begin{cases} 0.0000416\,T^3 - 0.027\,T^2 + 6.21\,T - 142.6 & \text{for}\ \ T < 270\text{K} \\ 0.1009\,T + 358.4 & \text{for}\ \ T \geq 270\text{K} \end{cases} \tag{2}$$

A constant specific heat (usually assumed to be 414 J/kg-K) is not appropriate at temperatures below 250 K and temperatures above 700 K, as can be seen from

Figure 1. The specific heat predicted by our model (equation (2)) is shown as a solid line in the figure. This model is used to compute the specific heat in all the simulations described in this paper.

The heat generated at a material point is conducted away at the end of a time step using the transient heat equation. The thermal conductivity of the material is assumed to be constant in our calculations. The effect of conduction on material point temperature is negligible for the high strain-rate problems simulated in this work. We have assumed a constant thermal conductivity of 386 W/(m-K) for copper which is the value at 500 K and atmospheric pressure.

2.2 Equation of State

The hydrostatic pressure (p) is calculated using a temperature-corrected Mie-Grüneisen equation of state of the form used by Zocher et al. (2000) (see also Wilkins (1999), p.61)

$$p = \frac{\rho_0 C_0^2 (\eta - 1)\left[\eta - \frac{\Gamma_0}{2}(\eta - 1)\right]}{\left[\eta - S_\alpha(\eta - 1)\right]^2} + \Gamma_0 E; \quad \eta = \frac{\rho}{\rho_0} \tag{3}$$

where C_0 is the bulk speed of sound, ρ_0 is the initial density, ρ is the current density, Γ_0 is the Grüneisen's gamma at reference state, $S_\alpha = dU_s/dU_p$ is a linear Hugoniot slope coefficient, U_s is the shock wave velocity, U_p is the particle velocity, and E is the internal energy per unit reference specific volume.

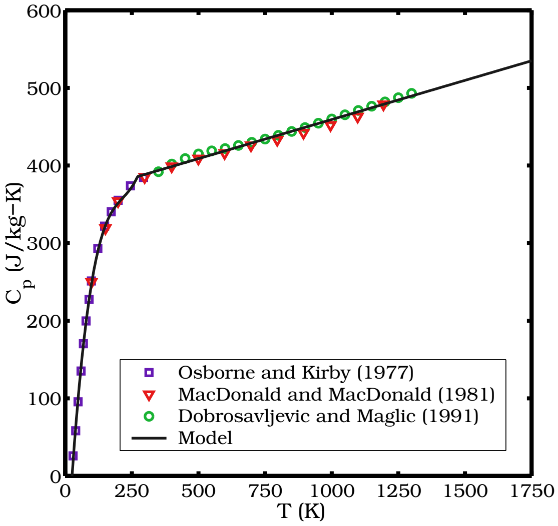

Fig. 1. Variation of the specific heat of copper with temperature. The solid line shows the values predicted by the model. Symbols show experimental data from Osborne and Kirby (1977), MacDonald and MacDonald (1981), and Dobrosavljevic and Maglic (1991).

The change in internal energy is computed using

$$E = \frac{1}{V_0} \int C_v dT \approx \frac{C_v (T - T_0)}{V_0} \tag{4}$$

where $V_0 = 1/\rho_0$ is the reference specific volume at temperature $T = T_0$, and C_v is the specific heat at constant volume. In our simulations, we assume that C_p and C_v are equal.

The hydrostatic pressure is used to compute the volumetric part of the Cauchy stress tensor in our simulations. The parameters that we use in the Mie-Grüneisen equation of state are shown in Table 1.

Figure 2 shows plots of the pressure predicted by the Mie-Grüneisen equation of state at three different temperatures. The reference temperature for these calculations is 300 K. An initial density ρ_0 of 8930 kg/m^3 has been used in the model calculations. The predicted pressures can be compared with pressures obtained from experimental shock Hugoniot data (shown by symbols in Figure 2). The model equation of state performs well for compressions less than 1.3. The pressures are underestimated at higher compression. We rarely reach compressions greater than 1.2 in our simulations. Therefore, the model that we have used is acceptable for our purposes.

2.3 Melting Temperature

The melting temperature model is used to determine the pressure-dependent melt temperature of copper. This melt temperature is used to compute the shear modulus and to flag the state (solid or liquid) of a particle. Two melting temperature models are evaluated in this paper. These are the Steinberg-Cochran-Guinan (SCG) melt model and the Burakovsky-Preston-Silbar (BPS) melt model.

Table 1

Parameters used in the Mie-Grüneisen EOS for copper. The bulk speed of sound and the slope of the linear fit to the Hugoniot for copper are from Mitchell and Nellis (1981). The value of the Grüneisen gamma is from MacDonald and MacDonald (1981).

C_0 (m/s)	S_α	Γ_0 ($T <$ 700 K)	Γ_0 ($T \geq$ 700 K)
3933	1.5	1.99	2.12

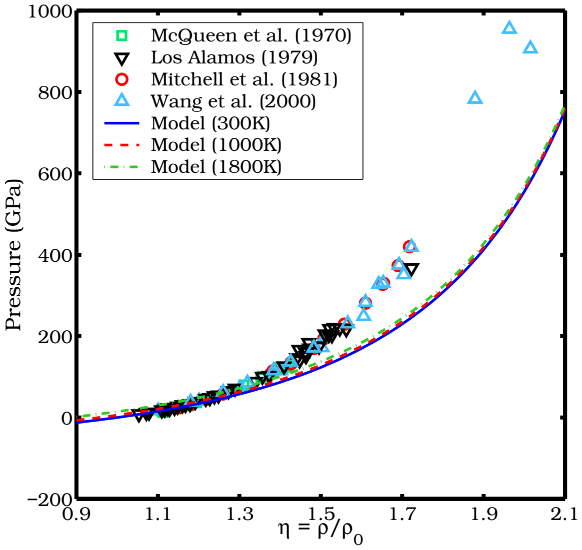

Fig. 2. The pressure predicted by the Mie-Grüneisen equation of state for copper as a function of compression. The continuous lines show the values predicted by the model for three temperatures. The symbols show experimental data obtained from McQueen et al. (1970), Marsh (1980), Mitchell and Nellis (1981), and Wang et al. (2000). The original sources of the experimental data can be found in the above citations.

2.3.1 *The Steinberg-Cochran-Guinan (SCG) melt model*

The Steinberg-Cochran-Guinan (SCG) melt model (Steinberg et al. (1980)) is a relation between the melting temperature (T_m) and the applied pressure. This model is based on a modified Lindemann law and has the form

$$T_m(\rho) = T_{m0} \exp\left[2a\left(1 - \frac{1}{\eta}\right)\right] \eta^{2(\Gamma_0 - a - 1/3)}; \qquad \eta = \frac{\rho}{\rho_0} \tag{5}$$

where T_{m0} is the melt temperature at $\eta = 1$, a is the coefficient of the first order volume correction to Grüneisen's gamma (Γ_0).

2.3.2 *The Burakovsky-Preston-Silbar (BPS) melt model*

An alternative melting relation that is based on dislocation-mediated phase transitions is the Burakovsky-Preston-Silbar (BPS) model (Burakovsky et al. (2000a)). The BPS model has the form

$$T_m(p) = T_m(0)\left[\frac{1}{\eta} + \frac{1}{\eta^{4/3}}\frac{\mu_0'}{\mu_0}\,p\right] \; ; \quad \eta = \left(1 + \frac{K_0'}{K_0}\,p\right)^{1/K_0'} \tag{6}$$

$$T_m(0) = \frac{\kappa\lambda\mu_0\, v_{WS}}{8\pi\ln(z-1)\; k_b}\ln\left(\frac{\alpha^2}{4\, b^2\rho_c(T_m)}\right) \tag{7}$$

where p is the pressure, η is the compression (determined using the Murnaghan equation of state), μ_0 is the shear modulus at room temperature and zero pressure, $\mu_0^{'} := \partial\mu/\partial p$ is the derivative of the shear modulus at zero pressure, K_0 is the bulk modulus at room temperature and zero pressure, $K_0^{'} := \partial K/\partial p$ is the derivative of the bulk modulus at zero pressure, κ is a constant, $\lambda := b^3/v_{WS}$ where b is the magnitude of the Burgers vector, v_{WS} is the Wigner-Seitz volume, z is the coordination number, α is a constant, $\rho_c(T_m)$ is the critical density of dislocations, and k_b is the Boltzmann constant.

2.3.3 *Evaluation of melting temperature models*

Table 2 shows the parameters used in the melting temperature models of copper. Figure 3 shows a comparison of the two melting temperature models along with experimental data from Burakovsky et al. (2000a) (shown as open circles). An initial density ρ_0 of 8930 kg/m^3 has been used in the model calculations.

Both models predict the melting temperature quite accurately for pressures below 50 GPa. The SCG model predicts melting temperatures that are closer to experimental values at higher pressures. However, the data at those pressures are sparse and should probably be augmented before conclusions regarding the models can be made. In any case, the pressures observed in our computations are usually less than 100 GPa and hence either model would suffice. We have chosen to use the SCG model for our copper simulations because the model is more computationally efficient than the BPS model.

Table 2
Parameters used in melting temperature models for copper. The parameter T_{m0} used in the SCG model is from Guinan and Steinberg (1974). The value of Γ_0 is from MacDonald and MacDonald (1981). The value of a has been chosen to fit the experimental data. The values of the initial bulk and shear moduli and their derivatives in the BPS model are from Guinan and Steinberg (1974). The remaining parameters for the BPS model are from Burakovsky and Preston (2000) and Burakovsky et al. (2000b).

Steinberg-Cochran-Guinan (SCG) model

T_{m0} (K)	Γ_0	a
1356.5	1.99	1.5

Burakovsky-Preston-Silbar (BPS) model

K_0 (GPa)	$K_0^{'}$	μ_0 (GPa)	$\mu_0^{'}$	κ	z	$b^2\rho_c(T_m)$	α	λ	v_{WS}	a (nm)
137	5.48	47.7	1.4	1.25	12	0.64	2.9	1.41	$a^3/4$	3.6147

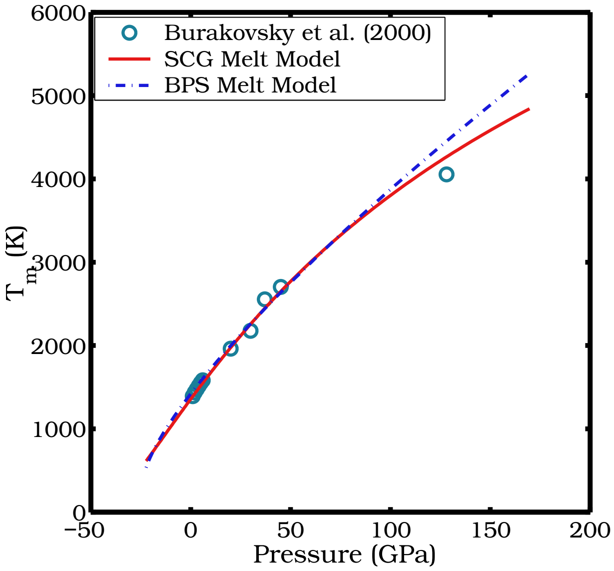

Fig. 3. The melting temperature of copper as a function of pressure. The lines show values predicted by the SCG and BPS models. The open circles show experimental data obtained from Burakovsky et al. (2000a). The original sources of the experimental data can be found in the above citation.

2.4 Shear Modulus

The shear modulus of copper decreases with temperature and is also pressure-dependent. The value of the shear modulus at room temperature is around 150% of the value close to melting. Hence, if we use the room temperature value of shear modulus for high temperature simulations we will overestimate the shear stiffness. This leads to the inaccurate estimation of the plastic strain-rate in radial return algorithms for elastic-plastic simulations. On the other hand, if the pressure-dependence of the shear modulus is neglected, modeling errors can accumulate for simulations involving shocks.

Three models for the shear modulus (μ) have been used in our simulations. The MTS shear modulus model was developed by Varshni (1970) and has been used in conjunction with the Mechanical Threshold Stress (MTS) flow stress model (Chen and Gray (1996); Goto et al. (2000a)). The Steinberg-Cochran-Guinan (SCG) shear modulus model was developed by Guinan and Steinberg (1974) and has been used in conjunction with the Steinberg-Cochran-Guinan-Lund (SCGL) flow stress model. The Nadal and LePoac (NP) shear modulus model (Nadal and Le Poac (2003)) is a recently developed model that uses Lindemann theory to determine the temperature dependence of shear modulus and the SCG model for pressure dependence.

2.4.1 MTS Shear Modulus Model

The MTS shear modulus model has the form (Varshni (1970); Chen and Gray (1996))

$$\mu(T) = \mu_0 - \frac{D}{exp(T_0/T) - 1} \tag{8}$$

where μ_0 is the shear modulus at 0K, and D, T_0 are material constants. The shortcoming of this model is that it does not include any pressure-dependence of the shear modulus and is probably not applicable for high pressure applications. However, the MTS shear modulus model does capture the flattening of the shear modulus-temperature curve at low temperatures that is observed in experiments.

2.4.2 SCG Shear Modulus Model

The Steinberg-Cochran-Guinan (SCG) shear modulus model (Steinberg et al. (1980); Zocher et al. (2000)) is pressure dependent and has the form

$$\mu(p,T) = \mu_0 + \frac{\partial \mu}{\partial p}\frac{p}{\eta^{1/3}} + \frac{\partial \mu}{\partial T}(T - 300); \quad \eta = \rho/\rho_0 \tag{9}$$

where, μ_0 is the shear modulus at the reference state(T = 300 K, p = 0, η = 1), p is the pressure, and T is the temperature. When the temperature is above T_m, the shear modulus is instantaneously set to zero in this model.

2.4.3 NP Shear Modulus Model

The Nadal-Le Poac (NP) shear modulus model (Nadal and Le Poac (2003)) is a modified version of the SCG model. The empirical temperature dependence of the shear modulus in the SCG model is replaced with an equation based on Lindemann melting theory. In addition, the instantaneous drop in the shear modulus at melt is avoided in this model. The NP shear modulus model has the form

$$\mu(p,T) = \frac{1}{\mathcal{J}(\hat{T})}\left[\left(\mu_0 + \frac{\partial \mu}{\partial p}\frac{p}{\eta^{1/3}}\right)(1 - \hat{T}) + \frac{\rho}{Cm}\,k_b\,T\right]; \quad C := \frac{(6\pi^2)^{2/3}}{3}f^2 \tag{10}$$

where

$$\mathcal{J}(\hat{T}) := 1 + \exp\left[-\frac{1 + 1/\zeta}{1 + \zeta/(1 - \hat{T})}\right] \quad \text{for} \quad \hat{T} := \frac{T}{T_m} \in [0, 1 + \zeta], \tag{11}$$

μ_0 is the shear modulus at 0 K and ambient pressure, ζ is a material parameter, k_b is the Boltzmann constant, m is the atomic mass, and f is the Lindemann constant.

2.4.4 Evaluation of shear modulus models

The parameters used in the three shear modulus models are given in Table 3. Figure 4(a) shows the shear modulus predicted by the MTS shear modulus model at zero hydrostatic pressure. It can be seen that the model fits the low temperature data quite well. The shear moduli predicted by the SCG and NP shear models are shown in Figure 4(b) and Figure 4(c), respectively. The SCG shear model predicts slightly different moduli than the NP model at different values of compression. Both models fit the experimental data quite well except at very low temperatures (at which the MTS model performs best). We have not be able to validate the pressure dependence of the shear modulus at high temperatures due to lack of experimental data. An initial density of 8930 kg/m^3 has been used in the model calculations.

3 Flow Stress Models

We have explored five temperature and strain-rate dependent models that can be used to compute the flow stress:

(1) the Johnson-Cook model
(2) the Steinberg-Cochran-Guinan-Lund model.
(3) the Zerilli-Armstrong model.
(4) the Mechanical Threshold Stress model.
(5) the Preston-Tonks-Wallace model.

The Johnson-Cook (JC) model (Johnson and Cook (1983)) is purely empirical and is the most widely used of the five. However, this model exhibits an unrealistically small strain-rate dependence at high temperatures. The

Table 3
Parameters used in shear modulus models for copper. The parameters for the MTS model have been chosen to fit the experimental data. The parameters for the SCG model are from Guinan and Steinberg (1974). The NP model parameters are from Nadal and Le Poac (2003).

MTS shear modulus model				SCG shear modulus model		
μ_0 (GPa)	D (GPa)	T_0 (K)		μ_0 (GPa)	$\partial\mu/\partial p$	$\partial\mu/\partial T$ (GPa/K)
51.3	3.0	165		47.7	1.3356	0.018126
NP shear modulus model						
μ_0 (GPa)	$\partial\mu/\partial p$	ζ	C	m (amu)		
50.7	1.3356	0.04	0.057	63.55		

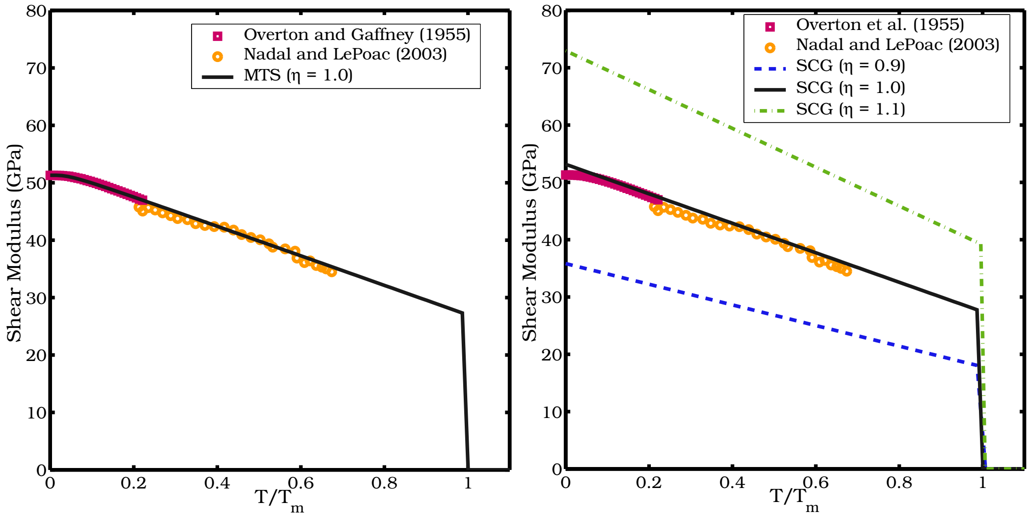

(a) MTS Shear Model

(b) SCG Shear Model

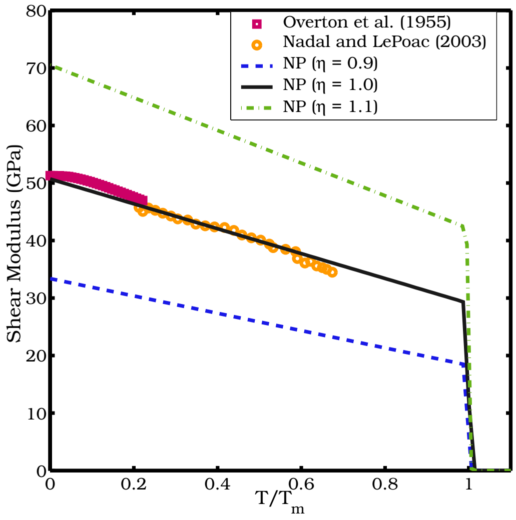

(c) NP Shear Model

Fig. 4. Shear modulus of copper as a function of temperature and pressure. The symbols represent experimental data from Overton and Gaffney (1955) and Nadal and Le Poac (2003). The lines show values of the shear modulus at different compressions ($\eta = \rho/\rho_0$).

Steinberg-Cochran-Guinan-Lund (SCGL) model (Steinberg et al. (1980); Steinberg and Lund (1989)) is semi-empirical. The model is purely empirical and strain-rate independent at high strain-rates. A dislocation-based extension based on Hoge and Mukherjee (1977) is used at low strain-rates. The SCGL model is used extensively by the shock physics community. The Zerilli-Armstrong (ZA) model (Zerilli and Armstrong (1987)) is a simple physically-based model that has been used extensively. A more complex model that is based on ideas from dislocation dynamics is the Mechanical Threshold Stress (MTS) model (Follansbee and Kocks (1988)). This model has been used to model the plastic deformation of copper, tantalum (Chen and Gray (1996)), alloys of steel (Goto et al. (2000a); Banerjee (2005a)), and aluminum alloys (Puchi-Cabrera et al. (2001)). However, the MTS model is limited to strain-rates less than around 10^7 /s. The Preston-Tonks-Wallace (PTW) model (Preston et al. (2003)) is also physically based and has a form similar to the MTS model. However, the PTW model has components that can model plastic deformation in the overdriven shock regime (strain-rates greater that 10^7 /s). Hence this model is valid for the largest range of strain-rates among the five flow stress models.

3.1 JC Flow Stress Model

The Johnson-Cook (JC) model (Johnson and Cook (1983)) is purely empirical and gives the following relation for the flow stress (σ_y)

$$\sigma_y(\epsilon_p, \dot{\epsilon}_p, T) = [A + B(\epsilon_p)^n] \left[1 + C \ln(\dot{\epsilon}_p^*)\right] [1 - (T^*)^m] \tag{12}$$

where ϵ_p is the equivalent plastic strain, $\dot{\epsilon}_p$ is the plastic strain-rate, and A, B, C, n, m are material constants.

The normalized strain-rate and temperature in equation (12) are defined as

$$\dot{\epsilon}_p^* := \frac{\dot{\epsilon}_p}{\dot{\epsilon}_{p0}} \qquad \text{and} \qquad T^* := \frac{(T - T_0)}{(T_m - T_0)} \tag{13}$$

where $\dot{\epsilon}_{p0}$ is a user defined plastic strain-rate, T_0 is a reference temperature, and T_m is a reference melt temperature. For conditions where $T^* < 0$, we assume that $m = 1$.

3.2 SCGL Flow Stress Model

The Steinberg-Cochran-Guinan-Lund (SCGL) model is a semi-empirical model that was developed by Steinberg et al. (1980) for high strain-rate situations and extended to low strain-rates and bcc materials by Steinberg and Lund (1989). The flow stress in this model is given by

$$\sigma_y(\epsilon_p, \dot{\epsilon}_p, T) = [\sigma_a f(\epsilon_p) + \sigma_t(\dot{\epsilon}_p, T)] \frac{\mu(p, T)}{\mu_0}; \quad \sigma_a f \le \sigma_{\text{max}} \text{ and } \sigma_t \le \sigma_p \tag{14}$$

where σ_a is the athermal component of the flow stress, $f(\epsilon_p)$ is a function that represents strain hardening, σ_t is the thermally activated component of the flow stress, $\mu(p, T)$ is the pressure- and temperature-dependent shear modulus, and μ_0 is the shear modulus at standard temperature and pressure. The saturation value of the athermal stress is σ_{max}. The saturation of the thermally activated stress is the

Peierls stress (σ_p). The shear modulus for this model is usually computed with the SCG shear modulus model.

The strain hardening function (f) has the form

$$f(\epsilon_p) = [1 + \beta(\epsilon_p + \epsilon_{pi})]^n \tag{15}$$

where β, n are work hardening parameters, and ϵ_{pi} is the initial equivalent plastic strain.

The thermal component (σ_t) is computed using a bisection algorithm from the following equation (citetHoge77,Steinberg89).

$$\dot{\epsilon}_p = \left[\frac{1}{C_1}\exp\left[\frac{2U_k}{k_b\,T}\left(1 - \frac{\sigma_t}{\sigma_p}\right)^2\right] + \frac{C_2}{\sigma_t}\right]^{-1} ; \quad \sigma_t \le \sigma_p \tag{16}$$

where $2U_k$ is the energy to form a kink-pair in a dislocation segment of length L_d, k_b is the Boltzmann constant, σ_p is the Peierls stress. The constants C_1, C_2 are given by the relations

$$C_1 := \frac{\rho_d L_d a b^2 \nu}{2w^2}; \quad C_2 := \frac{D}{\rho_d b^2} \tag{17}$$

where ρ_d is the dislocation density, L_d is the length of a dislocation segment, a is the distance between Peierls valleys, b is the magnitude of the Burgers' vector, ν is the Debye frequency, w is the width of a kink loop, and D is the drag coefficient.

3.3 ZA Flow Stress Model

The Zerilli-Armstrong (ZA) model (Zerilli and Armstrong (1987, 1993); Zerilli (2004)) is based on simplified dislocation mechanics. The general form of the equation for the flow stress is

$$\sigma_y(\epsilon_p, \dot{\epsilon}_p, T) = \sigma_a + B\exp(-\beta(\dot{\epsilon}_p)T) + B_0\sqrt{\epsilon_p}\exp(-\alpha(\dot{\epsilon}_p)T)\ . \tag{18}$$

In this model, σ_a is the athermal component of the flow stress given by

$$\sigma_a := \sigma_g + \frac{k_h}{\sqrt{l}} + K\epsilon_p^n, \tag{19}$$

where σ_g is the contribution due to solutes and initial dislocation density, k_h is the microstructural stress intensity, l is the average grain diameter, K is zero for fcc materials, B, B_0 are material constants.

In the thermally activated terms, the functional forms of the exponents α and β are

$$\alpha = \alpha_0 - \alpha_1\ln(\dot{\epsilon}_p); \quad \beta = \beta_0 - \beta_1\ln(\dot{\epsilon}_p); \tag{20}$$

where $\alpha_0, \alpha_1, \beta_0, \beta_1$ are material parameters that depend on the type of material (fcc, bcc, hcp, alloys). The Zerilli-Armstrong model has been modified by Abed and Voyiadjis (2005) for better performance at high temperatures. However, we have not used the modified equations in our computations.

3.4 MTS Flow Stress Model

The Mechanical Threshold Stress (MTS) model (Follansbee and Kocks (1988); Goto et al. (2000b); Kocks (2001)) has the form

$$\sigma_y(\epsilon_p, \dot{\epsilon}_p, T) = \sigma_a + (S_i\sigma_i + S_e\sigma_e)\frac{\mu(p,T)}{\mu_0} \tag{21}$$

where σ_a is the athermal component of mechanical threshold stress, σ_i is the component of the flow stress due to intrinsic barriers to thermally activated dislocation motion and dislocation-dislocation interactions, σ_e is the component of the flow stress due to microstructural evolution with increasing deformation (strain hardening), (S_i, S_e) are temperature and strain-rate dependent scaling factors, and μ_0 is the shear modulus at 0 K and ambient pressure,

The scaling factors take the Arrhenius form

$$S_i = \left[1 - \left(\frac{k_b\,T}{g_{0i}b^3\mu(p,T)}\ln\frac{\dot{\epsilon}_{p0i}}{\dot{\epsilon}_p}\right)^{1/q_i}\right]^{1/p_i} \tag{22}$$

$$S_e = \left[1 - \left(\frac{k_b\,T}{g_{0e}b^3\mu(p,T)}\ln\frac{\dot{\epsilon}_{p0e}}{\dot{\epsilon}_p}\right)^{1/q_e}\right]^{1/p_e} \tag{23}$$

where k_b is the Boltzmann constant, b is the magnitude of the Burgers' vector, (g_{0i}, g_{0e}) are normalized activation energies, $(\dot{\epsilon}_{p0i}, \dot{\epsilon}_{p0e})$ are constant reference strain-rates, and (q_i, p_i, q_e, p_e) are constants.

The strain hardening component of the mechanical threshold stress (σ_e) is given by an empirical modified Voce law

$$\frac{d\sigma_e}{d\epsilon_p} = \theta(\sigma_e) \tag{24}$$

where

$$\theta(\sigma_e) = \theta_0[1 - F(\sigma_e)] + \theta_{IV} F(\sigma_e) \tag{25}$$

$$\theta_0 = a_0 + a_1 \ln \dot{\epsilon}_p + a_2 \sqrt{\dot{\epsilon}_p} - a_3 T \tag{26}$$

$$F(\sigma_e) = \frac{\tanh\left(\alpha \dfrac{\sigma_e}{\sigma_{es}}\right)}{\tanh(\alpha)} \tag{27}$$

$$\ln(\frac{\sigma_{es}}{\sigma_{0es}}) = \left(\frac{kT}{g_{0es} b^3 \mu(p,T)}\right) \ln\left(\frac{\dot{\epsilon}_p}{\dot{\epsilon}_{p0es}}\right) \tag{28}$$

and θ_0 is the hardening due to dislocation accumulation, θ_{IV} is the contribution due to stage-IV hardening, ($a_0, a_1, a_2, a_3, \alpha$) are constants, σ_{es} is the stress at zero strain hardening rate, σ_{0es} is the saturation threshold stress for deformation at 0 K, g_{0es} is a constant, and $\dot{\epsilon}_{p0es}$ is the maximum strain-rate. Note that the maximum strain-rate is usually limited to about 10^7/s.

3.5 PTW Flow Stress Model

The Preston-Tonks-Wallace (PTW) model (Preston et al. (2003)) attempts to provide a model for the flow stress for extreme strain-rates (up to 10^{11}/s) and temperatures up to melt. A linear Voce hardening law is used in the model. The PTW flow stress is given by

$$\sigma_y(\epsilon_p, \dot{\epsilon}_p, T) = \begin{cases} 2\left[\tau_s + \alpha \ln\left[1 - \varphi \exp\left(-\beta - \dfrac{\theta \epsilon_p}{\alpha \varphi}\right)\right]\right] \mu(p,T) & \text{thermal regime} \\ 2\tau_s \mu(p,T) & \text{shock regime} \end{cases} \tag{29}$$

with

$$\alpha := \frac{s_0 - \tau_y}{d}; \quad \beta := \frac{\tau_s - \tau_y}{\alpha}; \quad \varphi := \exp(\beta) - 1 \tag{30}$$

where τ_s is a normalized work-hardening saturation stress, s_0 is the value of τ_s at 0K, τ_y is a normalized yield stress, θ is the hardening constant in the Voce hardening law, and d is a dimensionless material parameter that modifies the Voce hardening law.

The saturation stress and the yield stress are given by

$$\tau_s = \max\left\{s_0 - (s_0 - s_\infty)\text{erf}\left[\kappa \hat{T} \ln\left(\frac{\gamma \dot{\xi}}{\dot{\epsilon}_p}\right)\right], s_0 \left(\frac{\dot{\epsilon}_p}{\gamma \dot{\xi}}\right)^{s_1}\right\} \tag{31}$$

$$\tau_y = \max\left\{y_0 - (y_0 - y_\infty)\text{erf}\left[\kappa \hat{T} \ln\left(\frac{\gamma \dot{\xi}}{\dot{\epsilon}_p}\right)\right], \min\left\{y_1 \left(\frac{\dot{\epsilon}_p}{\gamma \dot{\xi}}\right)^{y_2}, s_0 \left(\frac{\dot{\epsilon}_p}{\gamma \dot{\xi}}\right)^{s_1}\right\}\right\} \tag{32}$$

where s_∞ is the value of τ_s close to the melt temperature, (y_0, y_∞) are the values of τ_y at 0K and close to melt, respectively, (κ, γ) are material constants, $\hat{T} = T/T_m$, (s_1, y_1, y_2) are material parameters for the high strain-rate regime, and

$$\dot{\xi} = \frac{1}{2}\left(\frac{4\pi\rho}{3M}\right)^{1/3}\left(\frac{\mu(p,T)}{\rho}\right)^{1/2} \tag{33}$$

where ρ is the density, and M is the atomic mass.

3.6 Evaluation of flow stress models

In this section, we evaluate the flow stress models on the basis of one-dimensional tension and compression tests. The high rate tests have been simulated using the explicit Material Point Method Sulsky et al. (1994, 1995) (see Appenedix A) in conjunction with the stress update algorithm given in Appendix B. The quasistatic tests have been simulated with a fully implicit version of the Material Point Method (Guilkey and Weiss (2003)) with an implicit stress update (Simo and Hughes (1998)). Heat conduction is performed at all strain-rates. As expected, we obtain nearly isothermal conditions for the quasistatic tests and nearly adiabatic conditions for the high strain-rate tests. We have used a constant thermal conductivity of 386 W/(m-K) for copper which is the value at 500 K and atmospheric pressure. To damp out large oscillations in high strain-rate tests, we use a three-dimensional form of the von Neumann artificial viscosity (Wilkins (1999), p.29). The viscosity factor takes the form

$$q = C_0\,\rho\,l\,\sqrt{\frac{K}{\rho}}|\,\text{tr}\boldsymbol{D}| + C_1\,\rho\,l^2\;(\,\text{tr}\boldsymbol{D})^2 \tag{34}$$

where C_0 and C_1 are constants, ρ is the mass density, K is the bulk modulus, $\boldsymbol{D}$ is the rate of deformation tensor, and l is a characteristic length (usually the grid cell size). We have used $C_0 = 0.2$ and $C_1 = 2.0$ in all our simulations. The temperature-dependent specific heat model, the Mie-Grüneisen equation of state, and the SCG melting temperature model have been used in all the following simulations.

The predicted stress-strain curves are compared with experimental data for annealed OFHC copper from tension tests (Nemat-Nasser (2004) (p. 241-242)) and compression tests (Samanta (1971)). The data are presented in form of true stress versus true strain. Note that detailed verification has been performed to confirm the correct implementation of the models withing the Uintah code. Also note that the high strain-rate experimental data are suspect for strains less than 0.1. This is because the initial strain-rate fluctuates substantially in Kolsky-Hopkinson bar experiments.

3.6.1 Johnson-Cook Model.

The parameters that we have used in the Johnson-Cook (JC) flow stress model of annealed copper are given in Table 4. We have used the NP shear modulus model in simulations involving the JC model.

The Johnson-Cook model is independent of pressure. Hence, the predicted yield stress is the same in compression and tension. The use of a variable specific heat model leads to a reduced yield stress at 77 K for high strain rates. However, the effect is relatively small. At high temperatures, the effect of the higher specific heat is to reduce the rate of increase of temperature with increase in plastic strain. This effect is also small. The temperature dependence of the shear modulus does not affect the yield stress. However, it has a small effect on the value of the plastic strain-rate.

The solid lines in Figures 5(a) and (b) show predicted values of the yield stress for various strain-rates and temperatures. The symbols show the experimental data. The Johnson-Cook model overestimates the initial yield stress for the quasistatic (0.1/s strain-rate), room temperature (296 K), test. The rate of hardening is underestimated by the model for the room temperature test at 8000/s. The strain-rate dependence of the yield stress is underestimated at high temperature (see the data at 1173 K in Figure 5(a)). For the tests at a strain-rate of 4000/s (Figure 5(b)), the yield stress is consistently underestimated by the Johnson-Cook model.

3.6.2 Steinberg-Cochran-Guinan-Lund Model.

The parameters used in the Steinberg-Cochran-Guinan-Lund (SCGL) model of annealed OFHC copper are listed in Table 5. We have used the SCG shear modulus model in simulations involving the SCGL model. We could alternatively have used the NP shear modulus model. However, we use the SCG model to highlight a problem with the equivalence of $\partial\mu/\partial T$ and $\partial\sigma_y/\partial T$ that is assumed by the SCGL model. A bisection algorithm is used to determine the thermally activated part of the flow stress for low strain-rates (less than 1000/s).

The solid lines in Figures 6(a) and (b) show the flow stresses predicted by the SCGL model. Clearly, the softening associated with increasing temperature is underestimated by the SCGL model though the yield stress at 8000/s is predicted reasonably accurately. For the tests at 4000/s shown in Figure 6(b), the SCGL

Table 4
Parameters used in the Johnson-Cook model for copper (Johnson and Cook (1985)).

A (MPa)	B (MPa)	C	n	m	$\dot{\epsilon}_{p0}$ (/s)	T_0 (K)	T_m (K)
90	292	0.025	0.31	1.09	1.0	294	1356

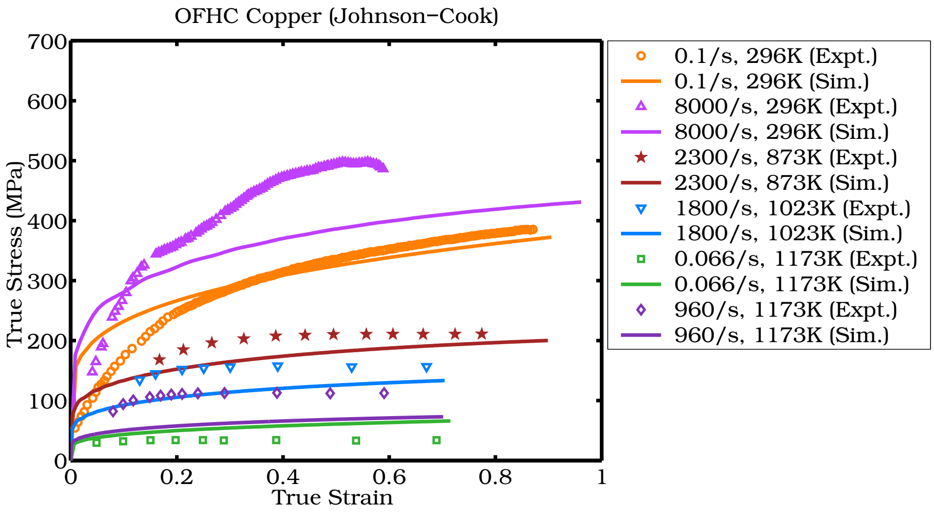

(a) Various strain-rates and temperatures.

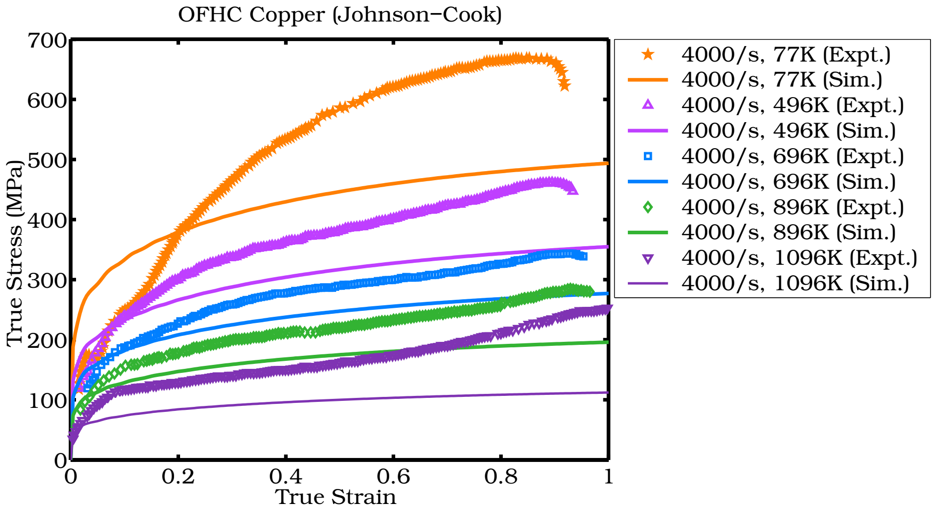

(b) Various temperatures at 4000/s strain-rate.

Fig. 5. Predicted values of yield stress from the Johnson-Cook model. The experimental data at 873 K, 1023 K, and 1173 K are from Samanta (1971) and represent compression tests. The remaining experimental data are from tension tests in Nemat-Nasser (2004). The solid lines are the predicted values.

modes performs progressively worse with increasing temperature.

Overall, at low temperatures, the high strain-rate predictions from the SCGL model match the experimental data best. This is not surprising since the original model by Steinberg et al. (1980) (SCG) was rate-independent and designed for high strain-rate applications. However, the low strain rate extension by Steinberg and Lund (1989) does not lead to good predictions of the yield stress of OFHC copper at low temperatures.

The high temperature response of the SCGL model is dominated by the shear

Table 5
Parameters used in the Steinberg-Cochran-Guinan-Lund model for copper. The parameters for the athermal part of the SCGL model are from Steinberg et al. (1980). The parameters for the thermally activated part of the model are from a number of sources. The estimate for the Peierls stress is based on Hobart (1965).

σ_a (MPa)	$\sigma_{\max}$ (MPa)	β	ϵ_{pi} (/s)	n	C_1 (/s)	U_k (eV)	σ_p (MPa)	C_2 (MPa-s)
125	640	36	0.0	0.45	0.71×10^6	0.31	20	0.012

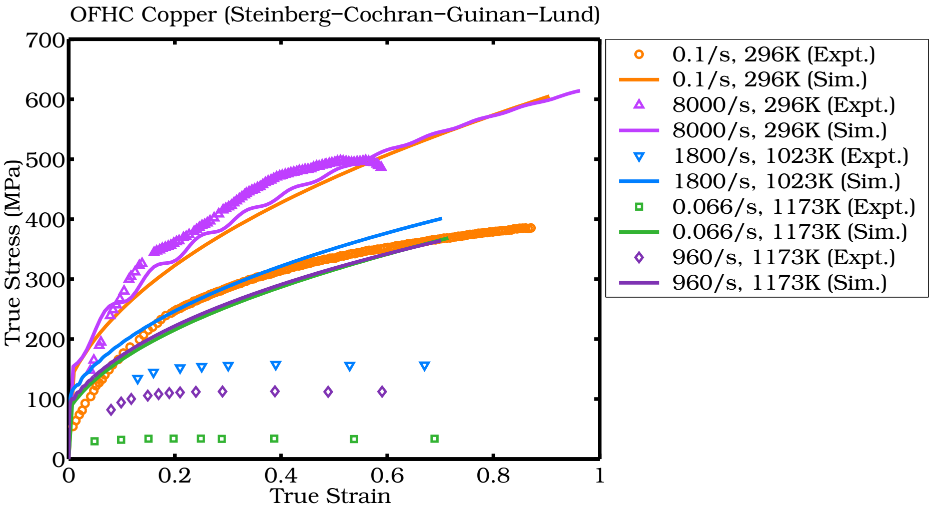

(a) Various strain-rates and temperatures.

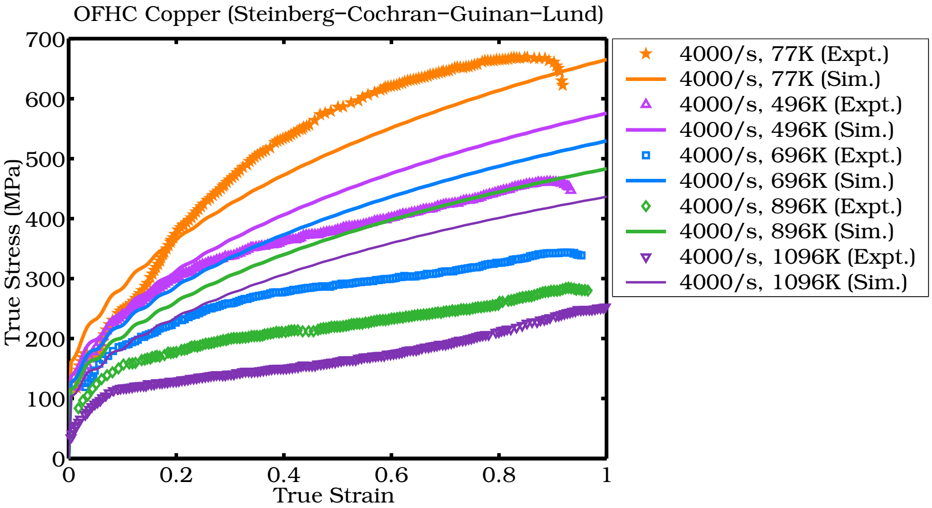

(b) Various temperatures at 4000/s strain-rate.

Fig. 6. Predicted values of yield stress from the Steinberg-Cochran-Guinan-Lund model. Please see the caption of Figure 5 for the sources of the experimental data.

modulus model; in particular, the derivative of the shear modulus with respect to temperature. From Figure 4(b) we can see that a value of -0.018126 GPa/K for $\partial\mu/\partial T$ matches the experimental data quite well. Steinberg et al. (1980) assume that the values of $(\partial\sigma_y/\partial T)/\sigma_{y0}$ and $(\partial\mu/\partial T)/\mu_0$ (-3.8×10-4 /K) are comparable. That does not appear to be the case for OFHC copper.

If we extract the yield stresses at a strain of 0.2 from the experimental data shown in Figure 6(b), we get the following values of temperature and yield stress for a strain-rate of 4000/s: (77 K, 380 MPa); (496 K, 300 MPa); (696 K, 230 MPa); (896 K, 180 MPa); (1096 K, 130 MPa). A straight line fit to the data shows that the value of $\partial\sigma_y/\partial T$ is -0.25 MPa/K. The yield stress at 300 K can be calculated from the fit to be approximately 330 MPa. This gives a value of -7.6×10$^-4$ /K for $(\partial\sigma_y/\partial T)/\sigma_{y0}$; approximately double the slope of the shear modulus versus temperature curve. Hence, a shear modulus derived from a shear modulus model cannot be used as a multiplier to the yield stress in equation (14). Instead, the original form of the SCG model (Steinberg et al. (1980)) must be used, with the term $(\partial\mu/\partial T)/\mu_0$ replaced by $(\partial\sigma_y/\partial T)/\sigma_{y0}$ in the expression for yield stress.

Figures 7(a) and (b) show the predicted yield stresses from the modified SCGL model. These plots show that there is a considerable improvement in the prediction of the temperature dependence of yield stress if the value of $(\partial\sigma_y/\partial T)/\sigma_{y0}$ is used instead of $(\partial\mu/\partial T)/\mu_0$. However, the strain-rate dependence of OFHC copper continues to be poorly modeled by the SCGL model.

3.6.3 Zerilli-Armstrong Model.

In contrast to the Johnson-Cook and the Steinberg-Cochran-Guinan models, the Zerilli-Armstrong (ZA) model for yield stress is based on dislocation mechanics and hence has some physical basis. The parameters used for the ZA model are given in Table 6. We have used the NP shear modulus model in our simulations that involve the ZA model.

Figures 8(a) and (b) show the yield stresses predicted by the ZA model. From Figure 8(a), we can see that the ZA model predicts the quasistatic, room temperature yield stress quite accurately. However, the room temperature yield

Table 6
Parameters used in the Zerilli-Armstrong model for copper (Zerilli and Armstrong (1987)).

σ_g (MPa)	k_h (MPa-mm$^{1/2}$)	l (mm)	K (MPa)	n	
46.5	5.0	0.073	0.0	0.5	
B (MPa)	β_0 (/K)	β_1 (s/K)	B_0 (MPa)	α_0 (/K)	α_1 (s/K)
0.0	0.0	0.0	890	0.0028	0.000115

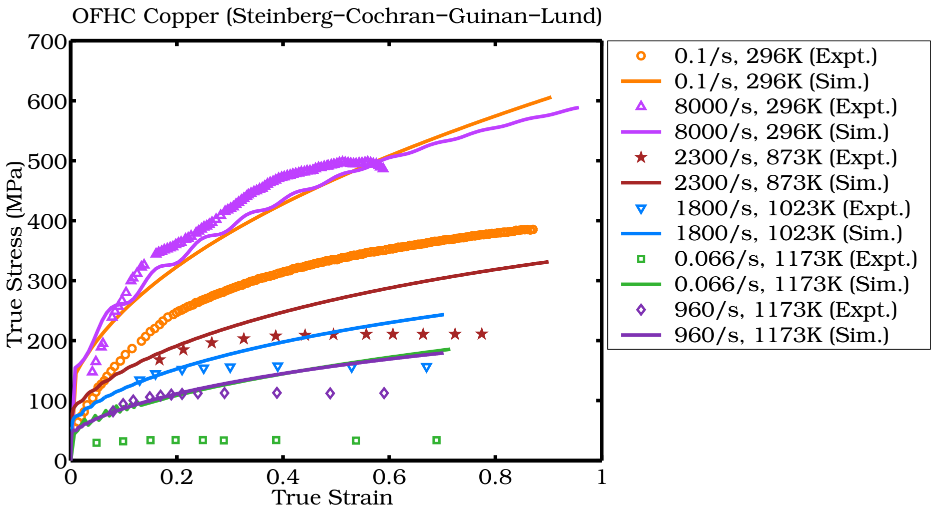

(a) Various strain-rates and temperatures.

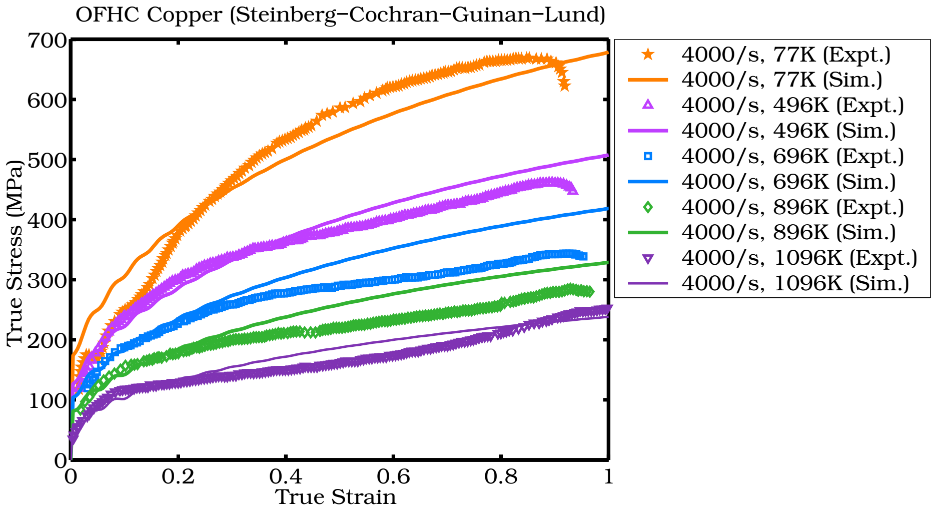

(b) Various temperatures at 4000/s strain-rate.

Fig. 7. Predicted values of yield stress from the modified Steinberg-Cochran-Guinan-Lund model. Please see the caption of Figure 5 for the sources of the experimental data.

stress at 8000/s is underestimated. The initial yield stress is overestimated at high temperatures; as are the saturation stresses.

Stress-strain curves at 4000/s are shown in Figure 8(b). In this case, the ZA model predicts reasonable initial yield stresses. However, the decrease in yield stress with increasing temperature is overestimated. We notice that the predicted yield stress at 496 K overlaps the experimental data for 696 K, while the predicted stress at 696 K overlaps the experimental data at 896 K.

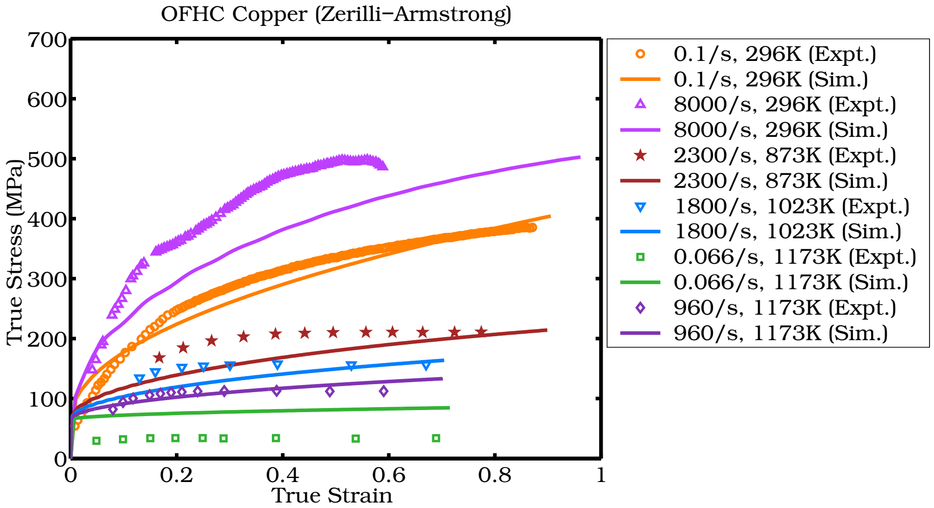

(a) Various strain-rates and temperatures.

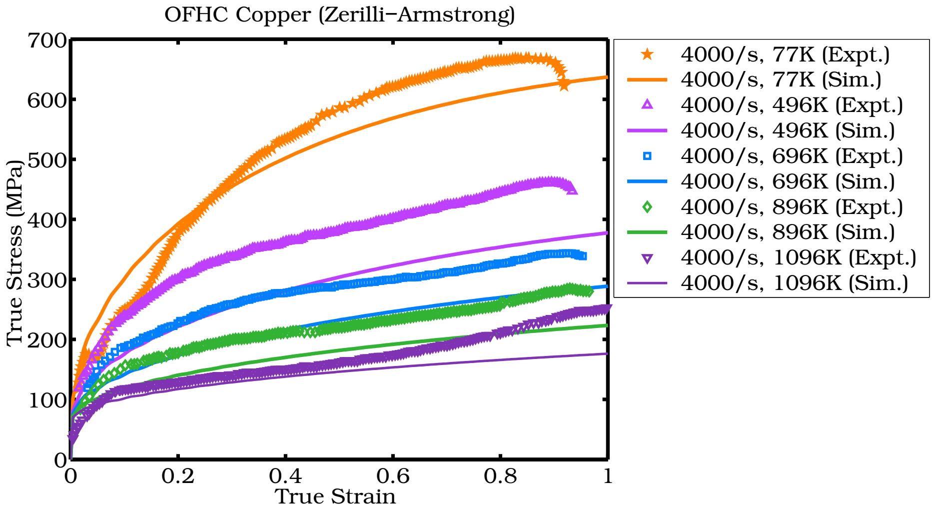

(b) Various temperatures and 4000/s strain-rate.

Fig. 8. Predicted values of yield stress from the Zerilli-Armstrong model. The symbols represent experimental data. The solid lines represented the computed stress-strain curves. Please see the caption of Figure 5 for the sources of the experimental data.

3.6.4 Mechanical Threshold Stress Model.

The Mechanical Threshold Stress (MTS) model is different from the three previous models in that the internal variable that evolves in time is a stress (σ_e). The value of the internal variable is calculated for each value of plastic strain by integrating equation (24) along a constant temperature and strain-rate path. An unconditionally stable and second-order accurate midpoint integration scheme has been used to determine the value of σ_e. Alternatively, an incremental update of the internal variable could be done using quantities from the previous timestep. The integration of the evolution equation is no longer along a constant temperature and strain-rate path in that case. We have found that two alternatives give us similar values of σ_e in the simulations that we have performed. The incremental update of the value of σ_e is considerably faster than the full update along a constant temperature and strain-rate path.

The parameters for the MTS model are shown in Table 7. The pressure-independent MTS shear modulus model has been used in simulations that use the MTS flow stress model. The reason for this choice is that the parameters of the model have been fit with such a shear modulus model. If the shear modulus model is changed, certain parameters of the model will have to be changed to reflect the difference.

Figures 9(a) and (b) show the experimental values of yield stress for OFHC copper versus those computed with the MTS model.

From Figure 9(a), we can see that the yield stress predicted by the MTS model almost exactly matches the experimental data at 296 K for a strain-rate of 0.1/s. The yield stress for the test conducted at 296 K and at 8000/s is underestimated. Though reasonably accurate yield stresses are predicted at 1023 K and 1800/s, the experimental curves exhibit earlier saturation than the model predicts. The same is true at 873 K and 2300 /s. The predicted yield stress is higher for the quasistatic test at 1173 K than that observed experimentally. However, the higher rate test at the same temperature matches the experiments quite well except for a higher amount of strain hardening at large strains.

The variation of yield stress with temperature at a strain-rate of 4000/s is shown in Figure 9(b). The figure shows that the yield stress is underestimated by the MTS model at all temperatures except 1096 K. The experimental data shows stage III or stage IV hardening which is not predicted by the MTS model that we have used.

3.6.5 Preston-Tonks-Wallace Model.

The Preston-Tonks-Wallace (PTW) model attempts to provide a single approach to model both thermally activated glide and overdriven shock regimes. The overdriven shock regime includes strain-rates greater than 10^7. The PTW model, therefore, extends the possibility of modeling plasticity beyond the range of validity of the MTS model. We have not conducted a simulations of overdriven shocks in this paper. However, the PTW model explicitly accounts for the rapid increase in yield stress at strain rates above 1000 /s. Hence the model is a good candidate for the range of strain-rates and temperatures of interest to us. The PTW model parameters used in our simulations are shown in Table 8. In addition, we use the NP shear modulus model in all simulations involving the PTW yield stress model.

Experimental yield stresses are compared with those predicted by the PTW model in Figures 10(a) and (b). The solid lines in the figures are the predicted values

Table 7
Parameters used in the Mechanical Threshold Stress model for copper (Follansbee and Kocks (1988)).

σ_a (MPa)	b (nm)	σ_i (MPa)	g_{0i}	$\dot{\epsilon}_{p0i}$ (/s)	p_i	q_i
40	0.256	0	1	1	1	1

g_{0e}	$\dot{\epsilon}_{p0e}$ (/s)	p_e	q_e	σ_{0es} (MPa)	g_{0es}	$\dot{\epsilon}_{p0es}$ (/s)
1.6	1.0×10^7	2/3	1	770	0.2625	1.0×10^7

α	a_0 (MPa)	a_1 (MPa-log(s))	a_2 (MPa-s$^{1/2}$)	a_3 (MPa/K)	θ_{IV} (MPa)
2	2390	12	1.696	0	0

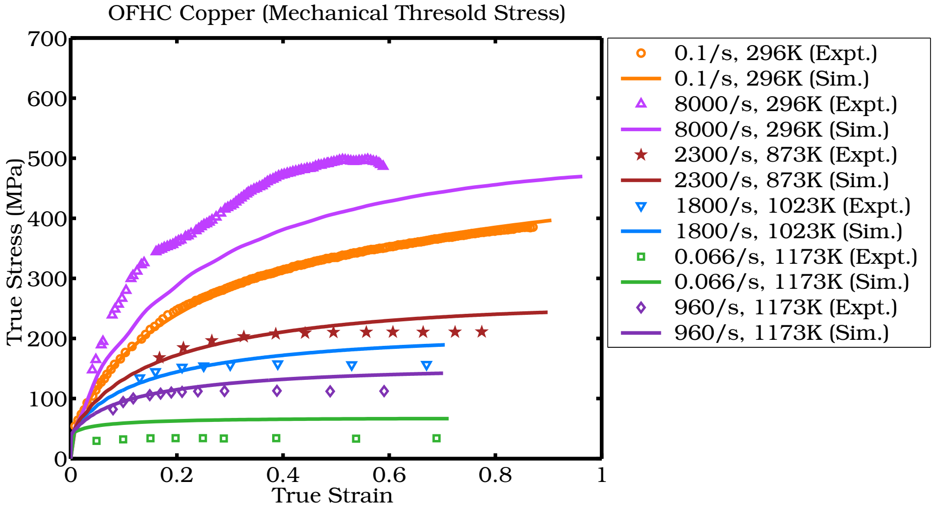

(a) Various strain-rates and temperatures.

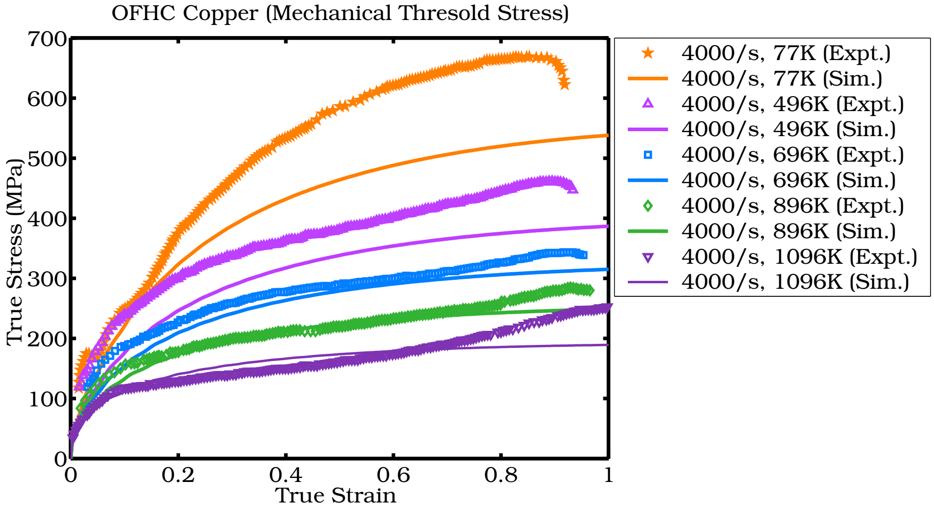

(b) Various temperatures at 4000/s strain-rate.

Fig. 9. Predicted values of yield stress from the Mechanical Threshold Stress model. Please see the caption of Figure 5 for the sources of the experimental data.

while the symbols represent experimental data. From Figure 10(a) we can see that the predicted yield stress at 0.1/s and 296 K matches the experimental data quite well. The error in the predicted yield stress at 296 K and 8000/s is also smaller than that for the MTS flow stress model. The experimental data at 873 K, 1023 K, and 1173 K were used by Preston et al. (2003) to fit the model parameters. Hence it is not surprising that the predicted yield stresses match the experimental data better than any other model.

The temperature-dependent yield stresses at 4000/s are shown in Figure 10(b). In this case, the predicted values at 77 K are lower than the experimental values. However, for higher temperatures, the predicted values match the experimental data quite well for strains less than 0.4. At higher strains, the predicted yield stress saturates while the experimental data continues to show a significant amount of hardening. The PTW model predicts better values of yield stress for the compression tests while the MTS model performs better for the tension tests.

3.6.6 Errors in the flow stress models.

In this section, we use the difference between the predicted and the experimental values of the flow stress as a metric to compare the various flow stress models. The error in the true stress is calculated using

$$\text{Error}_\sigma = \left(\frac{\sigma_{\text{predicted}}}{\sigma_{\text{expt.}}} - 1\right) \times 100 \; . \tag{35}$$

A detailed discussion of the differences between the predicted and experimental true stress for one-dimensional tests can be found elsewhere (Banerjee (2005b)). In this paper we summarize these differences in the form of error statistics as shown in Tables 9 and 10. Only true strains greater than 0.1 have been considered in the generation of these statistics. The statistics in Tables 9 and 10 clearly show that no single model is consistently better than the other models under all conditions.

We can further simplify our evaluation by considering a single metric that encapsulates much of the information in these tables. Table 11 shows comparisons based on one such simplified error metric. We call this metric the average maximum absolute (MA) error. The maximum absolute (MA) error is defined as the sum of the absolute mean error and the standard deviation of the error. The extreme values of the error are therefore ignored by the metric and only values that are within one standard deviation of the mean are considered.

From Table 11 we observe that the least average MA error for all the tests is 17% while the greatest average MA error is 64%. The PTW model performs best while the SCGL model performs worst. In order of increasing error, the models may be

Table 8
Parameters used in the Preston-Tonks-Wallace yield stress model for copper (Preston et al. (2003)).

s_0	s_∞	y_0	y_∞	d	κ	γ	θ
0.0085	0.00055	0.0001	0.0001	2	0.11	0.00001	0.025
M (amu)	s_1	y_1	y_2				
63.546	0.25	0.094	0.575				

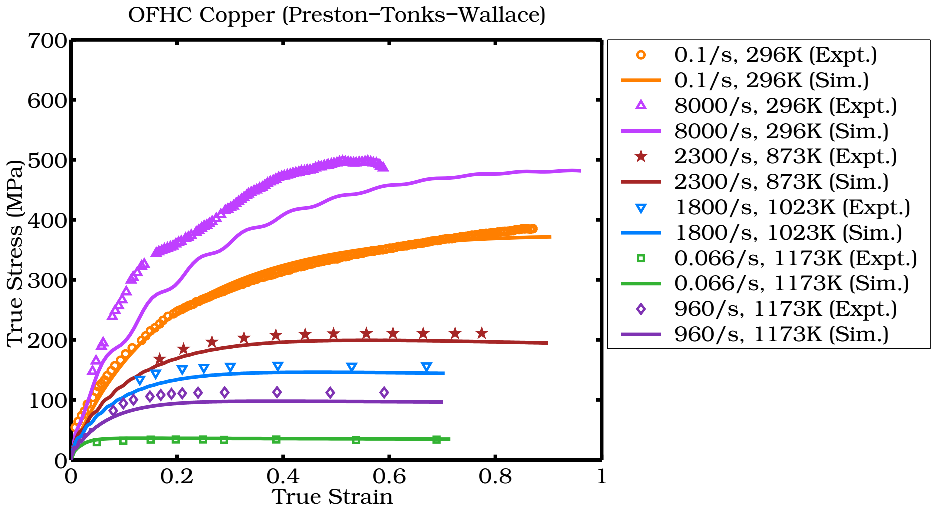

(a) Various strain-rates and temperatures.

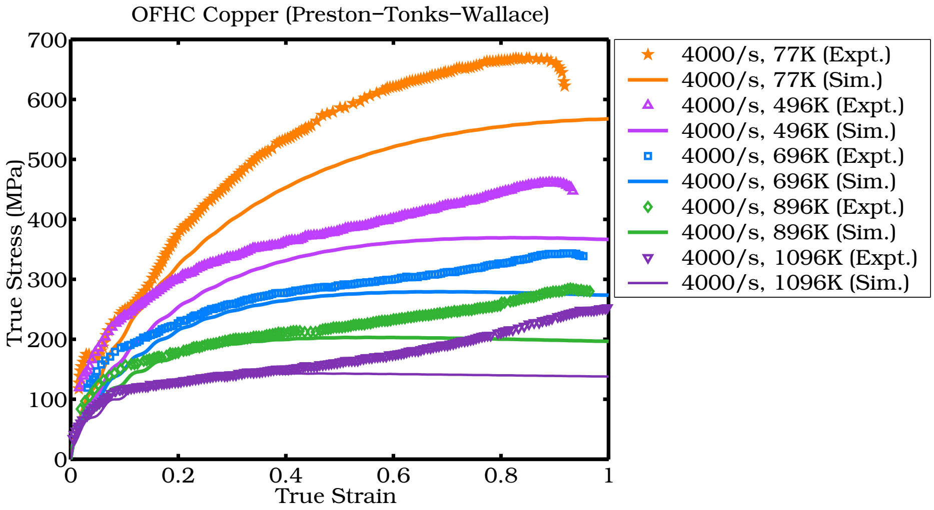

(b) Various temperatures at 4000/s strain-rate.

Fig. 10. Predicted values of yield stress from the Preston-Tonks-Wallace model. Please see the caption of Figure 5 for the sources of the experimental data.

Table 9
Comparison of the error in the yield stress predicted by the five flow stress models at various strain-rates and temperatures.

Temp. (K)	Strain Rate (/s)	Error	JC (%)	SCGL (%)	ZA (%)	MTS (%)	PTW (%)
296	0.1	Max.	32	55	3	2	3
		Min.	-4	31	-10	-4	-6
		Mean	0.2	41	-4	0.2	0.5
		Median	-3	41	-5	0.6	1.1
		Std. Dev.	6	7	4	1.3	2.3
296	8000	Max.	1.1	3	-10	-12	-6
		Min.	-22	-12	-21	-29	-29
		Mean	-17	-6	-17	-19	-14
		Median	-20	-7	-18	-18	-13
		Std. Dev.	6	3	2	3	4
873	2300	Max.	-7	49	-3	13	-5
		Min.	-18	6	-24	-5	-7
		Mean	-13	26	-15	4	-6
		Median	-13	25	-16	4	-6
		Std. Dev.	4	16	7	7	0.5
1023	1800	Max.	-16	53	3	20	-7
		Min.	-30	-3	-22	-7	-13
		Mean	-25	17	-13	4	-10
		Median	-27	11	-17	1.5	-9
		Std. Dev.	5	21	9	10	2
1173	0.066	Max.	93	440	149	99	7
		Min.	39	186	119	81	3
		Mean	64	297	132	90	5
		Median	61	275	131	92	6
		Std. Dev.	20	93	12	6	1.4
1173	960	Max.	-37	50	14	24	-13
		Min.	-49	-8	-8	-0.1	-17
		Mean	-45	12	-2	9	-15
		Median	-47	4	-6	6	-14
		Std. Dev.	4	20	8	9	1

Table 10
Comparison of the error in the yield stress predicted by the five flow stress models for a strain-rate of 4000/s.

Temp. (K)	Strain Rate (/s)	Error	JC (%)	SCGL (%)	ZA (%)	MTS (%)	PTW (%)
77	4000	Max.	34	26	24	-5	-8
		Min.	-28	-8	-9	-22	-17
		Mean	-14	-8	-2	-18	-15
		Median	-21	-4	-6	-19	-15
		Std. Dev.	16	9	9	5	2
496	4000	Max.	-2	11	-17	-11	-8
		Min.	-24	-7	-27	-26	-29
		Mean	-17	3	-22	-15	-14
		Median	-17	5	-21	-14	-13
		Std. Dev.	5	5	3	3	5
696	4000	Max.	-2	22	-16	-3	-4
		Min.	-20	-2	-25	-16	-20
		Mean	-14	13	-20	-6	-9
		Median	-15	15	-19	-6	-7
		Std. Dev.	4	7	3	3	5
896	4000	Max.	-16	20	-17	3	-2
		Min.	-32	-9	-24	-15	-30
		Mean	-23	13	-20	-3	-13
		Median	-21	16	-20	-2	-11
		Std. Dev.	4	7	2	5	9
1096	4000	Max.	-35	17	-8	12	4
		Min.	-56	-13	-30	-25	-45
		Mean	-42	7	-15	-1.4	-18
		Median	-39	9	-12	3	-15
		Std. Dev.	7	8	7	12	16

arranged as PTW, MTS, ZA, JC, and SCGL.

If we consider only the tension tests, we see that the MTS model performs best with an average MA error of 14%. The Johnson-Cook model does the worst at 25% error. For the compression tests, the PTW model does best with an error of

Table 11
Comparison of average ”maximum” absolute (MA) errors in yield stresses predicted by the five flow stress models for various conditions.

Condition	Average MA Error (%)				
	JC	SCGL	ZA	MTS	PTW
All Tests	36	64	33	23	17
Tension Tests	25	20	19	14	18
Compression Tests	45	126	50	35	10
High Strain Rate ($\geq$ 100 /s)	29	22	20	15	18
Low Strain Rate ($<$ 100 /s)	45	219	76	49	5
High Temperature ($\geq$ 800 K)	43	90	40	27	16
Low Temperature ($<$ 800 K)	20	20	17	15	14

10% compared to the next best, the MTS model with a 35% error. The SCGL error shows an average MA error of 126% for these tests.

For the high strain-rate tests, the MTS model performs better than the PTW model with an average MA error of 15% (compared to 18% for PTW). The low strain-rate tests are predicted best by the PTW model (5 %) and worst by the SCGL model (219 %). Note that this average error is based on two tests at 296 K and 1173 K and may not be representative for intermediate temperatures.

The PTW model shows an average MA error of 16% for the high temperature tests compared to 27% for the MTS model. The SCGL model again performs the worst. Finally, the low temperature tests ($<$ 800 K) are predicted best by the PTW model. The other models also perform reasonably well under these conditions.

From the above comparisons, the Preston-Tonks-Wallace and the Mechanical Threshold Stress models clearly stand out as reasonably accurate over the largest range of strain-rates and temperatures. To further improve our confidence in the above conclusions, we perform a similar set of comparisons with Taylor impact test data in the next section.

Note that we could potentially recalibrate all the models to get a better fit to the experimental data and render the above comparisons void. However, it is likely that the average user of such models in computational codes will use parameters that are readily available in the literature with the implicit assumption is that published parameters provide the best possible fit to experimental data. Hence, exercises such as ours provide useful benchmarks for the comparative evaluation of various flow stress models.

4 Taylor impact simulations

The Taylor impact test (Taylor (1948)) was originally devised as a means of determining the dynamic yield strength of solids. The test involves the impact of a flat-nosed cylindrical projectile on a hard target at normal incidence. The test was originally devised to determine the yield strengths of materials at high strain-rates. However, that use of the test is limited to peak strains of around 0.6 at the center of the specimen (Johnson and Holmquist (1988)). For higher strains and strain-rates, the Taylor test is more useful as a means of validating high strain-rate plasticity models in numerical codes (Zerilli and Armstrong (1987)).

The attractiveness of the Taylor impact test arises because of the simplicity and inexpensiveness of the test. A flat-ended cylinder is fired on a target at a relatively high velocity and the final deformed shape is measured. The drawback of this test is that intermediate states of the cylinder are relatively difficult to measure.

In this section, we compare the deformed profiles of Taylor cylinders from experiments with profiles that we obtain from our simulations. The experimental profiles are from the open literature and have been digitized at a high resolution. The errors in digitization are of the order of 2% to 5% depending on the clarity of the image. Our simulations use the Uintah code and the Material Point Method (see A and B).

All our simulations are three-dimensional and model a quarter of the cylinder. We have used 8 material points per cell (64 material points per cell for simulations at 1235 K), a 8 point interpolation from material points to grid, and a cell spacing of 0.3 mm. A cell spacing of 0.15 mm gives essentially the same final deformed profile (Banerjee (2005b)). The anvil is modeled as a rigid material. Contact between the cylinder and the anvil is assumed to be frictionless. The effect of frictional contact has been discussed elsewhere (Banerjee (2005b)). We have not included the effect of damage accumulation due to void nucleation and growth in these simulations. Details of such effects can be found in Banerjee (2005b).

Our simulations were run for 150 μs - 200 μs depending on the problem. These times were sufficient for the cylinders to rebound from the anvil and to stop undergoing further plastic deformation. However, small elastic deformations continue to persist as the stress waves reflect from the surfaces of the cylinder.

We have performed a systematic and extensive set of verification and validation tests to determine the accuracy of the Material Point Method and its implementation within Uintah (Banerjee (2004c,a,b, 2005c,a,b)). A number of materials and conditions have been explored in the process. We are, therefore, reasonably confident in the results of our simulations.

4.1 Metrics

The systematic verification and validation of computational codes and the associated material models requires the development and utilization of appropriate comparison metrics (see Oberkampf et al. (2002); Babuska and Oden (2004)). In this section we discuss a few geometrical metrics that can be used in the context of Taylor impact tests. Other metrics such as the surface temperature and the time of impact may also be used if measured values are available.

In most papers on the simulation of Taylor impact tests, a plot of the deformed configuration is superimposed on the experimental data and a visual judgement of accuracy is made. However, when the number of Taylor tests is large, it is not possible to present sectional/plan views for all the tests and numerical metrics are preferable. Some such metrics that have been used to compare Taylor impact tests are (see Figure 11) :

(1) The final length of the deformed cylinder (L_f) (Wilkins and Guinan (1973); Gust (1982); Jones and Gillis (1987); Johnson and Holmquist (1988); House et al. (1995)).
(2) The diameter of the mushroomed end of the cylinder (D_f) (Johnson and Holmquist (1988); House et al. (1995)).
(3) The length of the elastic zone in the cylinder (X_f) (Jones and Gillis (1987); House et al. (1995)).
(4) The bulge at a given distance from the deformed end (W_f) (Johnson and Holmquist (1988)).

Contours of plastic strain have also been presented in a number of works on Taylor impact. However, such contours are not of much use when comparing simulations with experiments (though they are useful when comparing two stress update algorithms).

The above metrics are inadequate when comparing the secondary bulges in two Taylor cylinders. We consider some additional geometrical metrics that act as a substitute for detailed pointwise geometrical comparisons between two Taylor test profiles. These are (see Figure 11) :

(1) The final length of a axial line on the surface of the cylinder (L_{af}).
(2) The area of the cross-sectional profile of the deformed cylinder (A_f).
(3) The volume of the deformed cylinder (V_f).
(4) The location of the centroid of the deformed cylinder in terms of a orthonormal basis with origin at deformed end (C_{xf}, C_{yf}).
(5) The moments of inertia of the cross section of the deformed cylinder about the basal plane (I_{xf}) and an axial plane (I_{yf}).

Higher order moments should also be computed so that we can dispense with

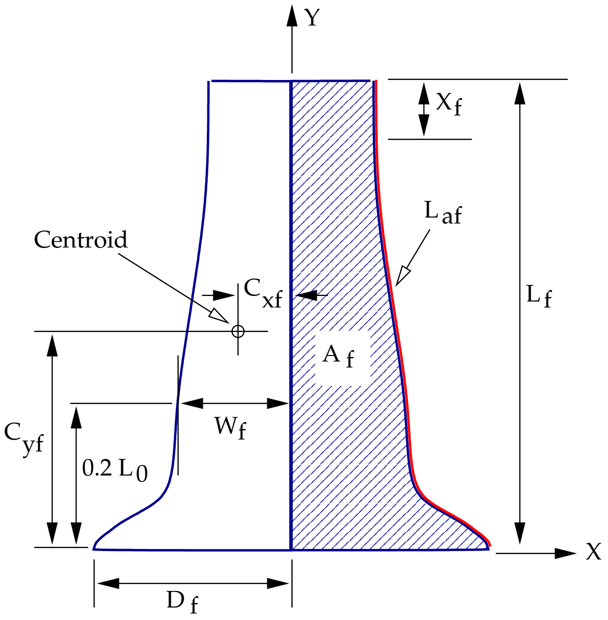

Fig. 11. Geometrical metrics used to compare profiles of Taylor impact specimens.

arbitrary measures such as W_f. The numerical formulas used to compute the area, volume, centroid, and moments of inertia are given in Appendix C.

4.2 Experimental data

In this section, we show plots of the experimentally determined values of some of the metrics discussed in the previous section. Quantities with subscript '0' represent initial values. The abscissa in each plot is a measure of the total energy density in the cylinder. The internal energy density has been added to the kinetic energy to separate the high temperature and low temperature data.

Figure 12 shows the length ratios (L_f/L_0) for a number of Taylor impact tests. The figure indicates the following:

(1) The ratio (L_f/L_0) is essentially independent of the initial length and diameter of the cylinder.
(2) There is a linear relationship between the ratio (L_f/L_0) and the initial kinetic energy density.
(3) As temperature increases, the absolute value of the slope of this line increases.
(4) The deformation of OFHC (Oxygen Free High Conductivity) cannot be distinguished from that of ETP (Electrolytic Tough Pitch) copper from this plot.

We have chosen to do detailed comparisons between experiment and simulation

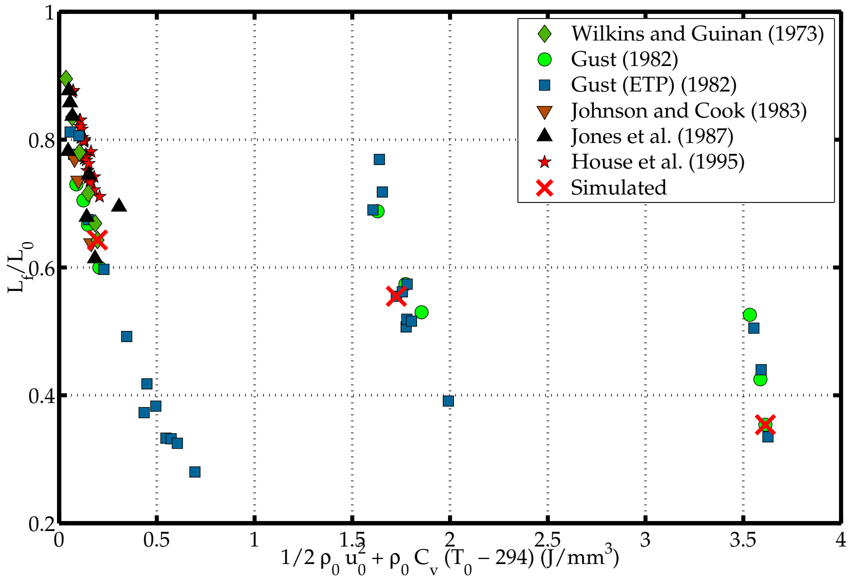

Fig. 12. Ratio of final length to initial length of copper Taylor cylinders for various conditions. The data are from Wilkins and Guinan (1973); Gust (1982); Johnson and Cook (1983); Jones and Gillis (1987) and House et al. (1995).

for the three tests marked with crosses on the figure. These tests represent situations in which fracture has not been observed in the cylinders and cover the range of temperatures of interest to us.

The ratio of the diameter of the deformed end to the original diameter (D_f/D_0) for some of these tests is plotted as a function of the energy density in Figure 13. A linear relation similar to that for the length is observed.

The volume of the cylinder should be preserved during the Taylor test if isochoric plasticity holds. Figure 14 shows the ratio of the final volume to the initial volume (V_f/V_0) as a function of the energy density. We can see that the volume is preserved for three of the tests but not for the rest. This discrepancy may be due to errors in digitization of the profile.

4.3 *Evaluation of flow stress models*

In this section we present results from simulations of three Taylor tests on copper, compute validation metrics, and compare these metrics with experimental data. Table 12 shows the initial dimensions, velocity, and temperature of the three specimens that we have simulated. All three specimens had been annealed before experimental testing.

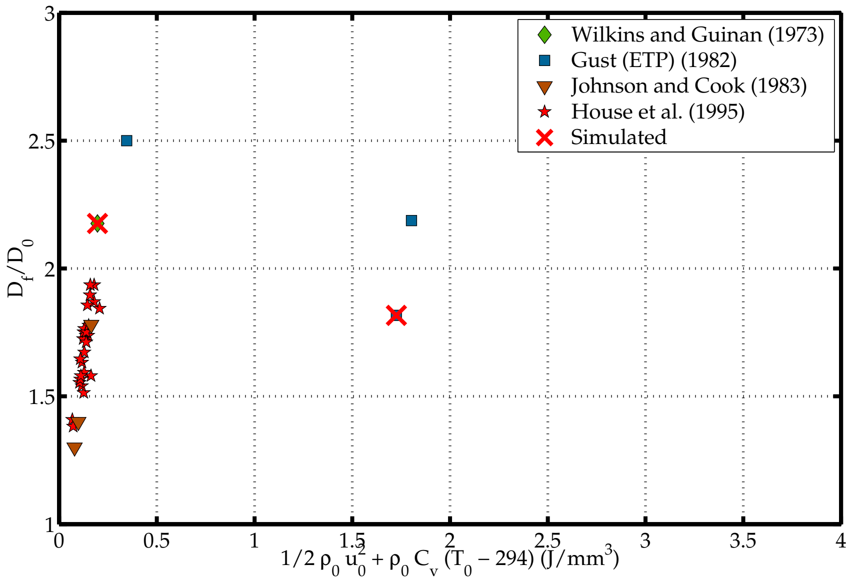

Fig. 13. Ratio of final length to initial length of copper Taylor cylinders for various conditions. The data are from Wilkins and Guinan (1973); Gust (1982); Johnson and Cook (1983) and House et al. (1995).

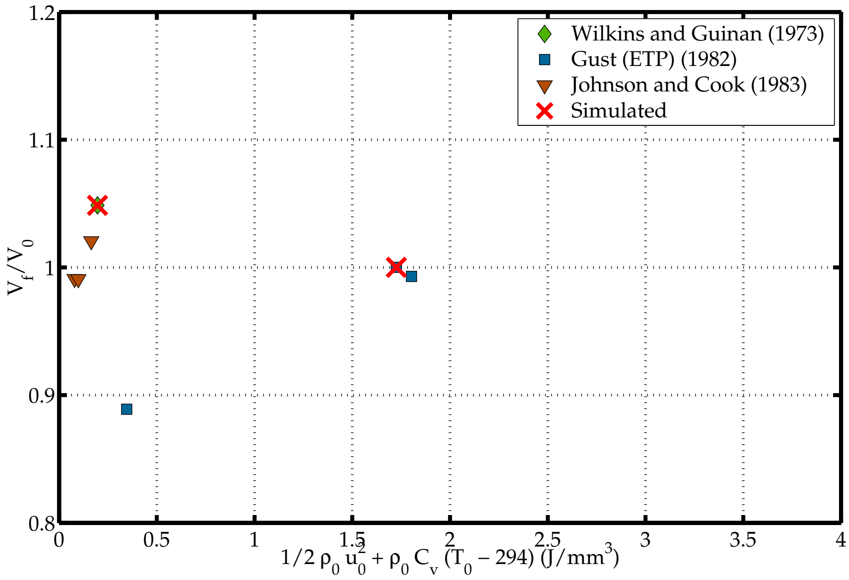

Fig. 14. Ratio of the final volume to initial volume of copper Taylor cylinders for various conditions. The data are from Wilkins and Guinan (1973); Gust (1982) and Johnson and Cook (1983).

4.3.1 Test Cu-1

Test Cu-1 is a room temperature test at an initial nominal strain-rate of around 9000/s. Figures 15(a), (b), (c), (d), and (e) show the profiles computed by the JC, SCGL, ZA, MTS, and PTW models, respectively, for test Cu-1.

Table 12
Initial data for copper simulations.

Test	Material	Initial Length (L_0 mm)	Initial Diameter (D_0 mm)	Initial Velocity (V_0 m/s)	Initial Temp. (T_0 K)	Source
Cu-1	OFHC Cu	23.47	7.62	210	298	Wilkins and Guinan (1973)
Cu-2	ETP Cu	30	6.00	188	718	Gust (1982)
Cu-3	ETP Cu	30	6.00	178	1235	Gust (1982)

The Johnson-Cook model gives the best match to the experimental data at this temperature (room temperature) if we consider the final length and the final mushroom diameter. All the other models underestimate the mushroom diameter but predict the final length quite accurately. The MTS model underestimates the final length.

The time at which the cylinder loses all its kinetic energy (as predicted by the models) is shown in the energy plot of Figure 15(f). The predicted times vary between 55 micro secs to 60 micro secs but are essentially the same for all the models. The total energy is conserved relatively well. The slight initial dissipation is the result of the artificial viscosity in the numerical algorithm that is used to damp out initial oscillations.

In Figure 14 we have seen that the final volume of the cylinder for test Cu-1 is around 5% larger than the initial volume. We assume that this error is due to errors in digitization. In that case, we have errors of +1% for measures of length and errors of +2% for measures of area in the experimental profile. Moments of inertia of areas are expected to have errors of around 7%.

The error metrics for test Cu-1 are shown in Figure 16. The final length (L_f) is predicted to within 3% of the experimental value by all the models. The Johnson-Cook and Preston-Tonks-Wallace models show the least error.

The length of the deformed surface of the cylinder (L_{af}) is predicted best by the Johnson-Cook and Steinberg-Cochran-Guinan-Lund models. The other models underestimate the length by more than 5%. The final mushroom diameter (D_f) is underestimated by 5% to 15%. The Johnson-Cook model does the best for this metric, followed by the Mechanical Threshold Stress model. The width of the bulge (W_f) is underestimated by the Johnson-Cook and SCGL models and accurately predicted by the ZA, MTS, and PTW models. The length of the elastic zone (X_f) is predicted to be zero by the SCGL, ZA, MTS, and PTW models while the Johnson-Cook model predicts a value of 1.5 mm. Moreover, an accurate estimate of X_f cannot be made from the experimental profile for test Cu-1. Therefore we do not consider this metric of utility in our comparisons for this test.

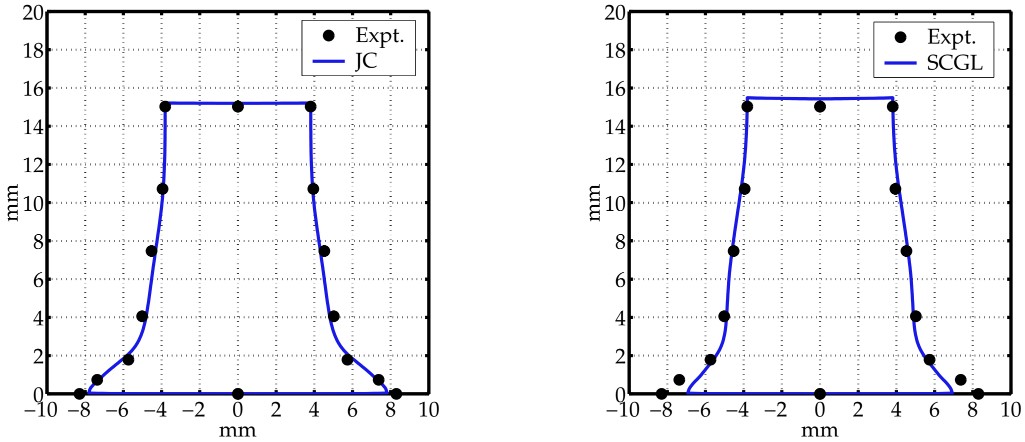

(a) Johnson-Cook.

(b) Steinberg-Cochran-Guinan-Lund.

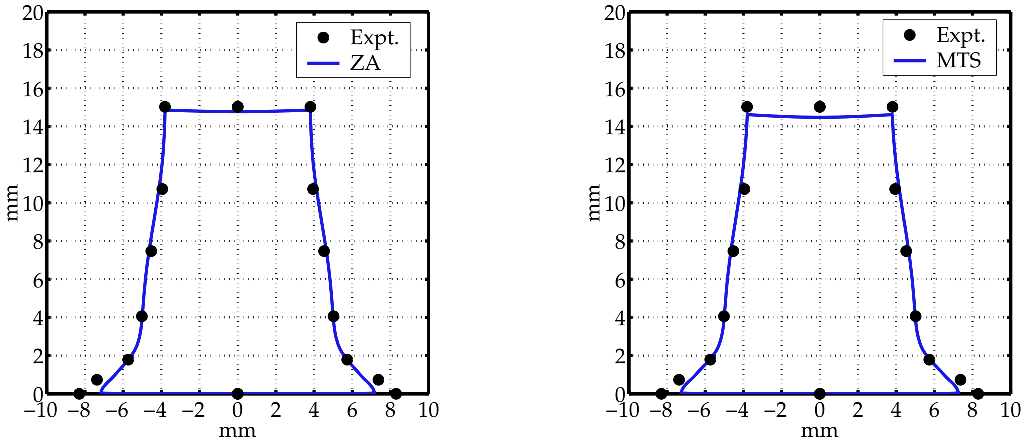

(c) Zerilli-Armstrong

(d) Mechanical Threshold Stress.

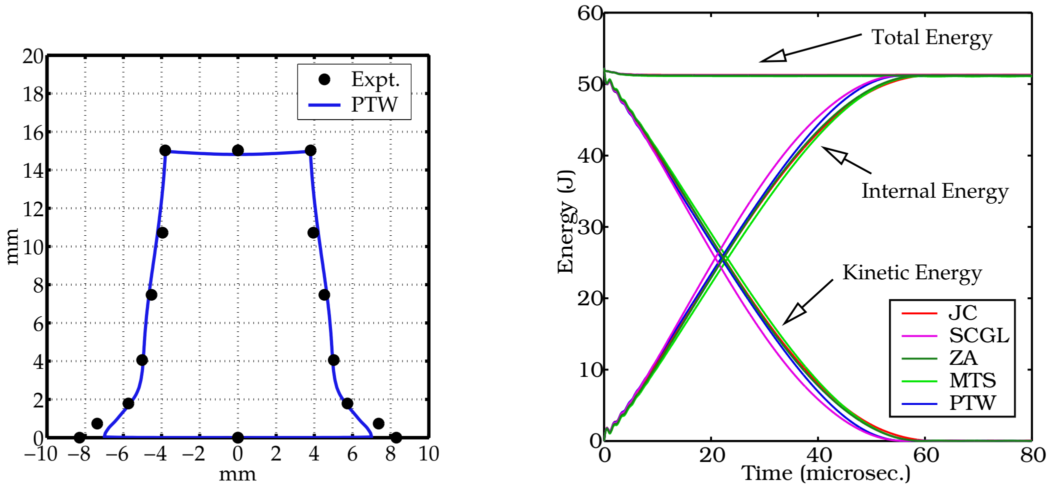

(e) Preston-Tonks-Wallace.

(f) Energy versus time.

Fig. 15. Computed versus experimental profiles for Taylor test Cu-1 and the computed energy versus time profile.

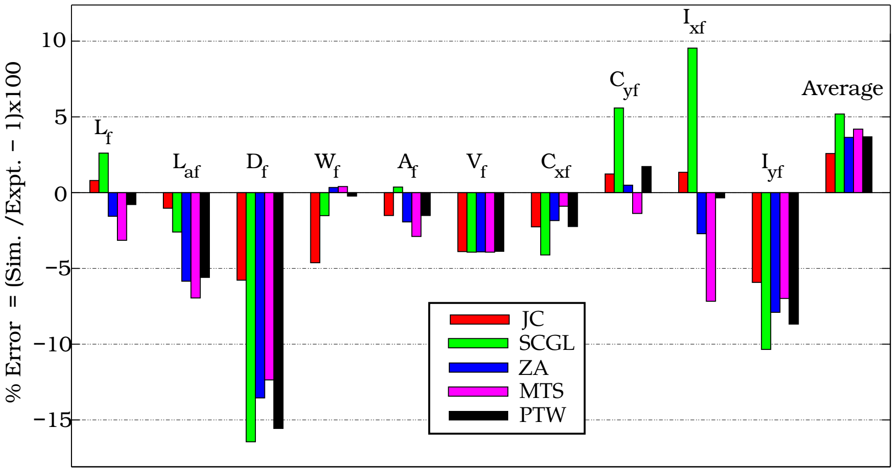

Fig. 16. Comparison of error metrics for the five models for Taylor test Cu-1.

From Figure 16 we see that the predicted area of the profile (A_f) is within 3% of the experimental value for all the models. The SCGL model shows the least error in this metric. If we decrease the experimental area by 2% (in accordance with the assumed error in digitization), the Johnson-Cook and PTW models show the least error in this metric.

The predicted final volume of the cylinder is around 0.8% larger than the initial volume showing that volume is not preserved accurately by our stress update algorithm. The error in digitization is around 5%. That gives us a uniform error of 5% between the experimental and computed volume (V_f) as can be seen in Figure 16.

The locations of the centroids (C_{xf}, C_{yf}) provide further geometric information about the shapes of the profiles. These are the first order moments of the area. The computed values are within 2% of experiment except for the MTS model which shows errors of -4% for C_{xf} and +6% for C_{yf}.

The second moments of the area are shown as I_{xf} and I_{yf} in Figure 16. The error in I_{xf} tracks and accentuates the error in L_f while the error in I_{yf} tracks the error in D_f. The width of the bulge is included in this metric and it can be used the replace metrics such as L_f, D_f, and W_f for the purpose of comparison. We notice this tracking behavior when the overall errors are small but not otherwise.

We have also plotted the arithmetic mean of the absolute value of the errors in each of the metrics to get an idea about which model performs best. The average error is the least (2.5%) for the Johnson-Cook model, followed by the ZA and PTW models (3.5%). The MTS model shows an average error of 4% while the SCGL model shows the largest error (5%). If we subtract the digitization error from the experimental values, these errors decrease and lie in the range of 2% to 3%.

In summary, all the models predict profiles that are within the range of experimental variation for the test at room temperature. Additional simulations at higher strain-rates (Banerjee (2005b)) have confirmed that all the models do well for room temperature simulations for strain rates ranging from 500 /s to 8000 /s. We suggest that the simplest model should be used for such room temperature simulations and our recommendation is the Zerilli-Armstrong model for copper.

4.3.2 Test Cu-2

Test Cu-2 is at a temperature of 718 K and the initial nominal strain-rate is around 6200/s. Figures 17(a), (b), (c), (d), and (e) show the profiles computed by the JC, SCGL, ZA, MTS, and PTW models, respectively, for test Cu-2.

In this case, the Johnson-Cook model predicts the final length well but overestimates the mushroom diameter. The SCGL model overestimates the length but predicts the mushroom diameter well. The ZA model predicts the overall profile remarkably well except for the mushroom diameter. The MTS model slightly overestimates both the final length and the mushroom diameter. The PTW model also performs similarly, except that the error is slightly larger than that for the MTS model.

The energy plot for test Cu-2 is shown in Figure 17(f). In this case, the time of impact predicted by the JC and ZA models is around 100 micro secs while that predicted by the SCGL, MTS, and PTW models is around 90 micro secs.

The error metrics for test Cu-2 are shown in Figure 18. In Figure 14 we have seen that the deformed volume computed from the digitized profile is almost exactly equal to the initial volume for test Cu-2. The digitization error can be neglected in this case.

The least error in the predicted final length (L_f) is for the ZA model followed by the JC model. The SCGL model shows the largest error in this metric (7%). The MTS and PTW models overestimate the final length by around 6%. The value of L_{af} is predicted to within 2% of the experimental value by the ZA model. The corresponding errors in the other models vary from 6% (MTS) to 9% (SCGL). The mushroom diameter is overestimated by all models. The JC model overestimates this metric by more than 30%. The ZA and PTW models overestimate D_f by 17% to 19%. The MTS model overestimates D_f by 12%. The SCGL model does best with an error of 7%. The width of the bulge is underestimated by all the models with errors varying between 5% (ZA) tp 9% (JC).

The final area (A_f) is predicted almost exactly by the JC model. The ZA model underestimates the area by 1% while the errors in the other models vary from 2% to 4%. The error in the final volume is less than 1% for all the models.

The location of the centroid is predicted best by the Johnson-Cook model followed

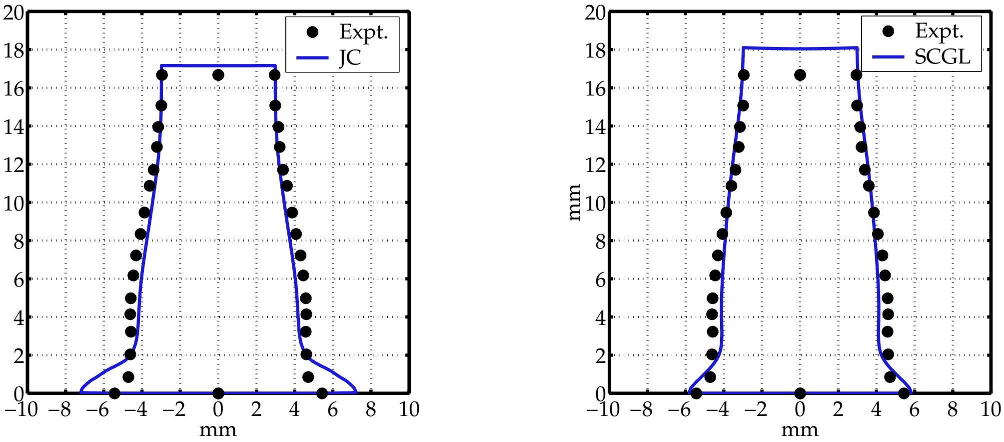

(a) Johnson-Cook.

(b) Steinberg-Cochran-Guinan-Lund.

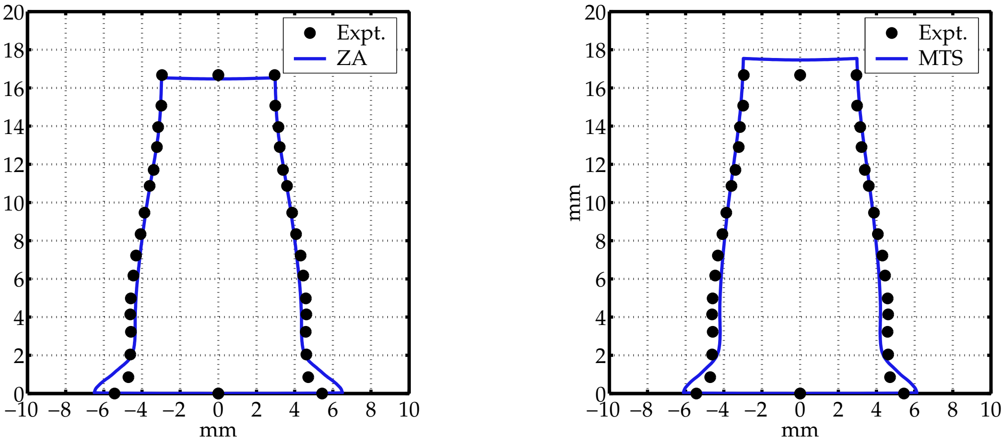

(c) Zerilli-Armstrong

(d) Mechanical Threshold Stress.

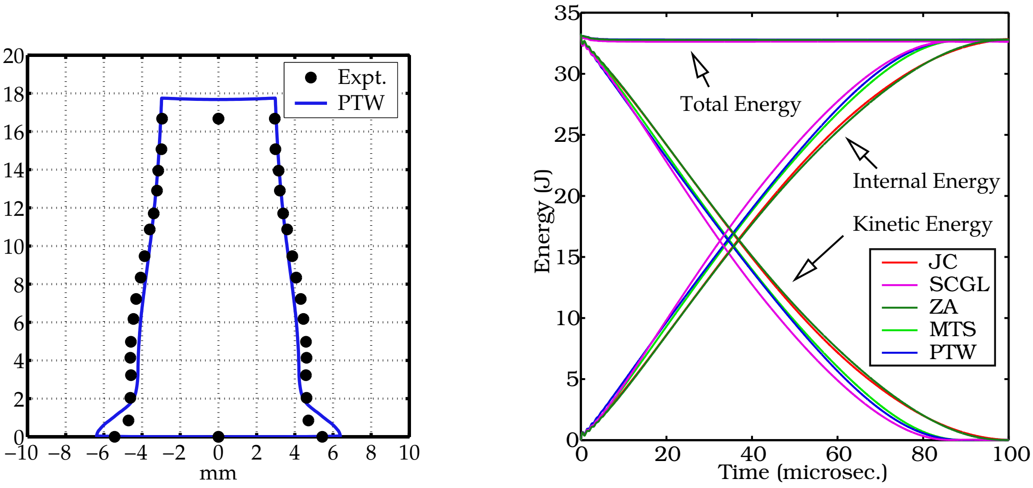

(e) Preston-Tonks-Wallace.

(f) Energy versus time.

Fig. 17. Computed and experimental profiles for Taylor test Cu-2 and the computed energy-time profile.

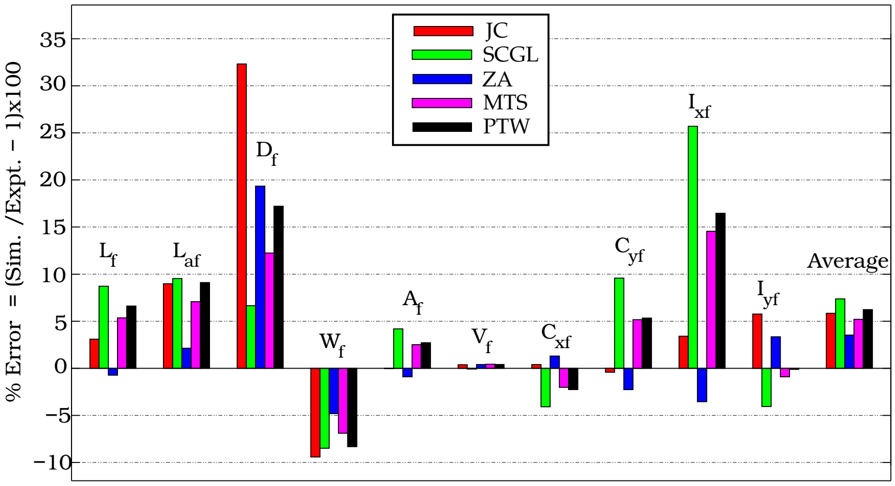

Fig. 18. Comparison of error metrics for the five models for Taylor test Cu-2.

by the ZA model. Both the MTS and PTW models underestimate C_{xf} by 2% and overestimate C_{yf} by 5%. The SCGL model shows the largest error for this metric.

For the second order moments I_{xf}, the smallest error is for the Johnson-Cook model followed by the ZA model. The largest errors are from the SCGL model. The MTS and PTW models overestimate this metric my 15%. The PTW model predicts I_{yf} the best, followed by the MTS model showing that the overall shape of the profile is best predicted by these models. The Johnson-Cook and SCGL models show the largest errors in this metric.

On average, the ZA model performs best for test Cu-2 at 718 K with an average error of 4%. The MTS model shows an average error of 5% while the JC and PTW models show errors of approximately 6%. The SCGL model, with an average error of approximately 7%, does the worst.

4.3.3 Test Cu-3

Test Cu-3 was conducted at 1235 K and at a initial nominal strain-rate of approximately 6000 /s. Figures 19(a), (b), (c), (d), and (e) show the profiles computed using the JC, SCGL, ZA, MTS, and PTW models, respectively. The complete experimental profile of the cylinder was not available for this test.

The Johnson-Cook model fails to predict a the deformation of the cylinder at this temperature and the material appears to flow along the plane of impact. The SCGL model predicts a reasonably close value of the final length. However, the low strain-rate part of the SCGL model behaves in an unstable manner at some levels of discretization for this test and should ideally be discarded in high strain-rate simulations. The ZA model overestimates the final length as does the MTS model. The PTW model predicts a final length that is closer to experiment but does not show the bulge that is characteristic of hardening. This can be seen from the tendency of the model to saturate prematurely as discussed in the section on one-dimensional tests.

The energy plot for test Cu-3 is shown in Figure 19(f). For this test, the JC model predicts a time of impact greater than 250 micro secs while the rest of the models predict values between 120 micro secs and 130 micro secs. The reason for the anomalous behavior of the JC model is that the rate dependence of the yield stress at high temperature is severely underestimated by the JC model. The nominal strain-rate is around 5000/s for this test at which the yield stress should be considerably higher than the 50 MPa that is computed by the JC model.

We do not have the final profile of the sample for this test and hence cannot compare any metrics other than the final length. The final length is predicted most accurately by the SCGL model with an error of 10%, followed by the PTW model (error 15%) and the ZA model (error 20%). The Johnson-Cook model shown an error of more than 90%.

These three sets of tests show that the performance of the models deteriorates with increasing temperature. However, on average all the models predict reasonably accurate profiles for the Taylor impact tests. The choice of the model should therefore be dictated by the required computational efficiency and the conditions expected during simulations.

5 Summary and conclusions

We have compared five flow stress models that are suitable for use in high strain-rate and high temperature simulations using one-dimensional tension/compression tests and Taylor impact tests. We have also evaluated the associated models for shear modulus, melting temperature, and the equation of state. We observe that during the simulation of large plastic deformations at high strain-rates and high temperatures, the following should be taken into consideration:

(1) The specific heat can be assumed constant when the range of temperatures is small. However, at temperatures below 250 K or above 750 K, the room temperature value of the specific heat may not be appropriate.

(2) The Mie-Grüneisen equation of state that we have used is valid only up to compressions of 1.3. A higher order approximation should be used if extreme pressures are expected during the simulation. We note that care should be exercised when this equation of state is used for states of large hydrostatic tension.

(3) The physically-based Burakovsky-Preston-Silbar melt temperature model should be used when the material is not well characterized. However, the

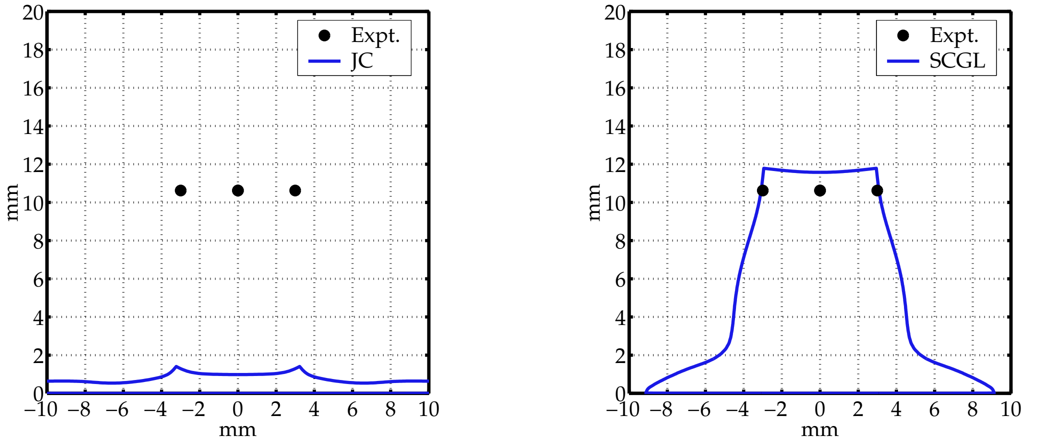

(a) Johnson-Cook.

(b) Steinberg-Cochran-Guinan-Lund.

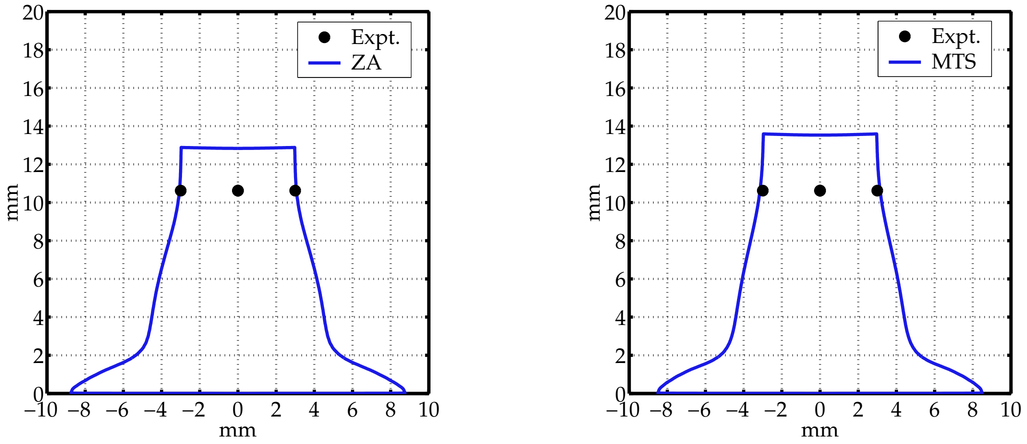

(c) Zerilli-Armstrong

(d) Mechanical Threshold Stress.

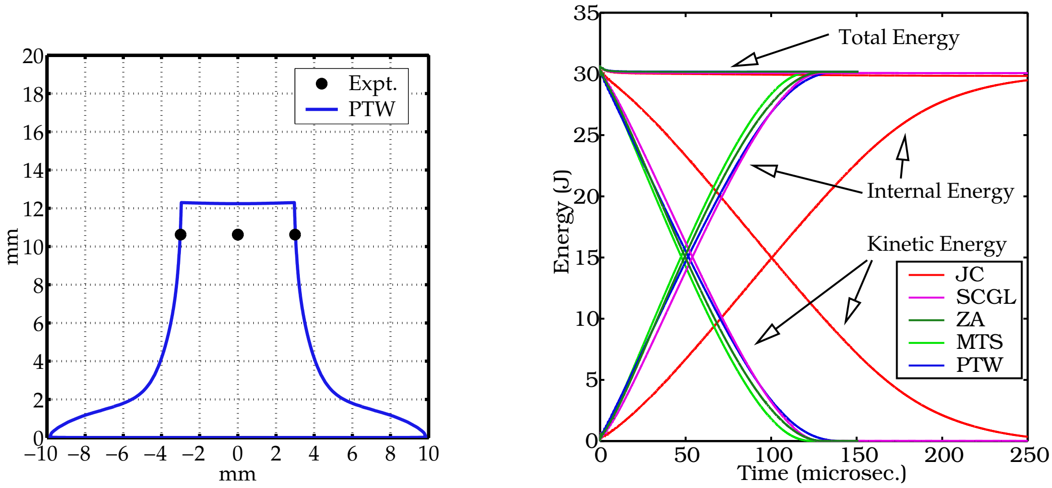

(e) Preston-Tonks-Wallace.

(f) Energy vs. time.

Fig. 19. Computed and experimental profiles for Taylor test Cu-3 and the computed energy-time profiles.

Steinberg-Cochran-Guinan model is quite accurate for copper and slightly less computationally expensive.

(4) The Nadal-Le Poac shear modulus model is the most robust model for high-temperature high-pressure applications. However, this model (as well as the Steinberg-Cochran-Guinan model) can be unreliable at high hydrostatic tensions. The MTS shear modulus model is the best at temperatures less than 200 K though it is inaccurate at high pressures.

(5) The Johnson-Cook (JC) flow stress model predicts that the strain-rate dependence of the yield stress is insignificant at high temperatures. This is inaccurate and the model should be recalibrated for high temperature applications.

(6) The contribution of the rate-dependent part of the Steinberg-Cochran-Guinan-Lund (SCGL) model to the total flow stress is small enough to be insignificant because it is limited by a constant Peierls stress. The model makes the assumption that $\partial\sigma_y/\partial T = \partial\mu/\partial T$. This assumption clearly does not hold for copper. If the model is corrected, the high strain-rate yield stresses are predicted quite accurately by the model.

(7) The Zerilli-Armstrong (ZA) model is quite accurate at low strain-rates. The temperature-dependence of the yield stress predicted by the model is larger than the actual value at high strain-rates with some exceptions.

(8) The Mechanical Threshold Stress (MTS) model shows the correct temperature dependence of the yield stress and high temperatures and strain-rates. The model is also quite accurate at low strain-rates. However, the stage-IV hardening at large tensile strains is not predicted by the model.

(9) The Preston-Tonks-Wallace (PTW) model is also quite accurate at both low and high strain-rates and at high temperatures. However, the predicted yield stress saturates at a tensile strains of 0.4 and the model represents stage-IV hardening worse than the Mechanical Threshold Stress model.

(10) The overall error for one-dimensional tests is least for the PTW model. For the tension tests, the MTS model is the most accurate while the PTW model is the most accurate for compression tests. The MTS model is the most accurate at high strain-rates while the PTW model is the most accurate at low strain-rates. The PTW model is the most accurate for both high- and low-temperature tests at all strain-rates.

(11) For comparing Taylor impact tests, geometric moments of the profile are better measures of the shape than arbitrary measures such as the width of the bulge at a fixed distance from the end.

(12) At room temperature, all the flow stress models predict the final profile of a Taylor impact cylinder quite accurately. At 718 K, the ZA model is the most accurate, followed by the MTS model. At 1235 K, the JC model fails to predict the final profile while the modified SCGL and the PTW models predict the final length most accurately. The PTW model fails to predict the bulge due to hardening at this temperature due to early saturation of the yield stress.

We conclude that no single model can accurately predict the yield stress for the full range of conditions considered in this study. Care should be exercised when choosing the models to be used in a particular simulation. If needed, the model should be recalibrated for the range of conditions of interest.

Acknowledgments

This work was supported by the the U.S. Department of Energy through the Center for the Simulation of Accidental Fires and Explosions, under grant W-7405-ENG-48.

A The Material Point Method

The Material Point Method (MPM) Sulsky et al. (1994, 1995) is a particle method for solid mechanics simulations. In this method, the state variables of the material are described on Lagrangian particles or “material points”. In addition, a regular, structured Eulerian grid is used as a computational scratch pad to compute spatial gradients and to solve the governing conservation equations. The explicit time-stepping version of the Material Point Method is summarized below.

It is assumed that an particle state at the beginning of a time step is known. The mass (m), external force ($\boldsymbol{f}^{\text{ext}}$), and velocity ($\boldsymbol{v}$) of the particles are interpolated to the grid using the relations

$$m_g = \sum_p S_{gp}\, m_p \ , \quad \boldsymbol{v}_g = (1/m_g) \sum_p S_{gp}\, m_p\, \boldsymbol{v}_p \ , \quad \boldsymbol{f}_g^{\text{ext}} = \sum_p S_{gp}\, \boldsymbol{f}_p^{\text{ext}} \tag{A.1}$$

where the subscript ‘g’ indicates a quantity at a grid node and a subscript ‘p’ indicates a quantity on a particle. The symbol $\sum_p$ indicates a summation over all particles. The quantity (S_{gp}) is the interpolation function of node g evaluated at the position of particle p.

Next, the velocity gradient at each particle is computed using the grid velocities using the relation

$$\boldsymbol{\nabla}\boldsymbol{v}_p = \sum_g \boldsymbol{G}_{gp}\boldsymbol{v}_g \tag{A.2}$$

where $\boldsymbol{G}_{gp}$ is the gradient of the shape function of node g evaluated at the position of particle p. The velocity gradient at each particle is used to determine the Cauchy stress ($\boldsymbol{\sigma}_p$) at the particle using a stress update algorithm.

The internal force at the grid nodes ($\boldsymbol{f}_g^{\text{int}}$) is calculated from the divergence of the stress using

$$\boldsymbol{f}_g^{\text{int}} = \sum_p \boldsymbol{G}_{gp}\, \boldsymbol{\sigma}_p\, V_p \tag{A.3}$$

where V_p is the particle volume.

The equation for the conservation of linear momentum is next solved on the grid. This equation can be cast in the form

$$\boldsymbol{m}_g\, a_g = \boldsymbol{f}_g^{\text{ext}} - \boldsymbol{f}_g^{\text{int}} \tag{A.4}$$

where $\boldsymbol{a}_g$ is the acceleration vector at grid node g.

The velocity vector at node g is updated using an explicit (forward Euler) time integration, and the particle velocity and position are then updated using grid quantities. The relevant equations are

$$\boldsymbol{v}_g(t+\Delta t) = \boldsymbol{v}_g(t) + \boldsymbol{a}_g\, \Delta t \tag{A.5}$$

$$\boldsymbol{v}_p(t+\Delta t) = \boldsymbol{v}_p(t) + \sum_g S_{gp}\, \boldsymbol{a}_g\, \Delta t\ ; \quad \boldsymbol{x}_p(t+\Delta t) = \boldsymbol{x}_p(t) + \sum_g S_{gp}\, \boldsymbol{v}_g\, \Delta t \tag{A.6}$$

The above sequence of steps is repeated for each time step. The above algorithm leads to particularly simple mechanisms for handling contact. Details of the interpolants and the contact algorithms can be found in Bardenhagen et al. (2001) and Bardenhagen and Kober (2004). The implicit version of the Material Point method can be found in Guilkey and Weiss (2003).

B Stress Update Algorithm

A modified form of a hypoelastic-plastic, semi-implicit elastic-plastic stress update algorithm (Nemat-Nasser (1991); Nemat-Nasser and Chung (1992); Wang and Atluri (1994); Maudlin and Schiferl (1996); Zocher et al. (2000)) has been used for the stress update in the simulations presented in this paper. Details of the socket-based objected oriented form of the complete algorithm can be found in Banerjee (2005b). We provide a brief description here for the sake of completeness.

Following Maudlin and Schiferl (1996), the rotated spatial rate of deformation tensor ($\boldsymbol{d}$) is decomposed into an elastic part ($\boldsymbol{d}^e$) and a plastic part ($\boldsymbol{d}^p$)

$$\boldsymbol{d} = \boldsymbol{d}^e + \boldsymbol{d}^p \tag{B.1}$$

If we assume plastic incompressibility ($\text{tr}(\boldsymbol{d}^p) = 0$), we get

$$\boldsymbol{\eta} = \boldsymbol{\eta}^e + \boldsymbol{\eta}^p \tag{B.2}$$

where $\boldsymbol{\eta}$, $\boldsymbol{\eta}^e$, and $\boldsymbol{\eta}^p$ are the deviatoric parts of $\boldsymbol{d}$, $\boldsymbol{d}^e$, and $\boldsymbol{d}^p$, respectively. For isotropic materials, the hypoelastic constitutive equation for deviatoric stress is

$$\dot{\boldsymbol{s}} = 2\mu(\boldsymbol{\eta} - \boldsymbol{\eta}^p) \tag{B.3}$$

where $\boldsymbol{s}$ is the deviatoric part of the stress tensor and μ is the shear modulus. We assume that the flow stress obeys the Huber-von Mises yield condition

$$f := \sqrt{\frac{3}{2}}\|\boldsymbol{s}\| - \sigma_y \leq 0 \;\text{ or, }\; F := \frac{3}{2}\boldsymbol{s} : \boldsymbol{s} - \sigma_y^2 \leq 0 \tag{B.4}$$

where σ_y is the flow stress. Assuming an associated flow rule, and noting that $\boldsymbol{d}^p = \boldsymbol{\eta}^p$, we have

$$\boldsymbol{\eta}^p = \boldsymbol{d}^p = \lambda\frac{\partial f}{\partial \boldsymbol{\sigma}} = \Lambda\frac{\partial F}{\partial \boldsymbol{\sigma}} = 3\Lambda\boldsymbol{s} \tag{B.5}$$

where $\boldsymbol{\sigma}$ is the stress. Let $\boldsymbol{u}$ be a tensor proportional to the plastic straining direction, and define γ as

$$\boldsymbol{u} = \sqrt{3}\frac{\boldsymbol{s}}{\|\boldsymbol{s}\|}; \quad \gamma := \sqrt{3}\Lambda\|\boldsymbol{s}\| \quad \Longrightarrow \gamma\boldsymbol{u} = 3\Lambda\boldsymbol{s} \tag{B.6}$$

Therefore, we have

$$\boldsymbol{\eta}^p = \gamma\boldsymbol{u}; \quad \dot{\boldsymbol{s}} = 2\mu(\boldsymbol{\eta} - \gamma\boldsymbol{u}) \tag{B.7}$$

From the consistency condition, if we assume that the deviatoric stress remains constant over a timestep, we get

$$\gamma = \frac{\boldsymbol{s} : \boldsymbol{\eta}}{\boldsymbol{s} : \boldsymbol{u}} \tag{B.8}$$

which provides an initial estimate of the plastic strain-rate. To obtain a semi-implicit update of the stress using equation (B.7), we define

$$\tau^2 := \frac{3}{2}\boldsymbol{s} : \boldsymbol{s} = \sigma_y^2 \tag{B.9}$$

Taking a time derivative of equation (B.9) gives us

$$\sqrt{2}\dot{\tau} = \sqrt{3}\frac{\boldsymbol{s} : \dot{\boldsymbol{s}}}{\|\boldsymbol{s}\|} \tag{B.10}$$

Plugging equation (B.10) into equation $(\text{B.7})_2$ we get

$$\dot{\tau} = \sqrt{2}\mu(\boldsymbol{u} : \boldsymbol{\eta} - \gamma\boldsymbol{u} : \boldsymbol{u}) = \sqrt{2}\mu(d - 3\gamma) \tag{B.11}$$

where $d = \boldsymbol{u} : \boldsymbol{\eta}$. If the initial estimate of the plastic strain-rate is that all of the deviatoric strain-rate is plastic, then we get an approximation to γ, and the corresponding error (γ_{er}) given by

$$\gamma_{\text{approx}} = \frac{d}{3}; \quad \gamma_{\text{er}} = \gamma_{\text{approx}} - \gamma = \frac{d}{3} - \gamma \tag{B.12}$$

The incremental form of the above equation is

$$\Delta\gamma = \frac{d^*\Delta t}{3} - \Delta\gamma_{\text{er}} \tag{B.13}$$

Integrating equation (B.11) from time t_n to time $t_{n+1} = t_n + \Delta t$, and using equation (B.13) we get

$$\tau_{n+1} = \tau_n + \sqrt{2}\mu(d^*\Delta t - 3\Delta\gamma) = \tau_n + 3\sqrt{2}\mu\Delta\gamma_{\text{er}} \tag{B.14}$$

where d^* is the average value of d over the timestep. Solving for $\Delta\gamma_{\text{er}}$ gives

$$\Delta\gamma_{\text{er}} = \frac{\tau_{n+1} - \tau_n}{3\sqrt{2}\mu} = \frac{\sqrt{2}\sigma_y - \sqrt{3}\|\boldsymbol{s}_n\|}{6\mu} \tag{B.15}$$

The direction of the total strain-rate ($\boldsymbol{u}^\eta$) and the direction of the plastic strain-rate ($\boldsymbol{u}^s$) are given by

$$\boldsymbol{u}^\eta = \frac{\boldsymbol{\eta}}{\|\boldsymbol{\eta}\|}; \quad \boldsymbol{u}^s = \frac{\boldsymbol{s}}{\|\boldsymbol{s}\|} \tag{B.16}$$

Let θ be the fraction of the time increment that sees elastic straining. Then

$$\theta = \frac{d^* - 3\gamma_n}{d^*} \tag{B.17}$$

where $\gamma_n = d_n/3$ is the value of γ at the beginning of the timestep. We also assume that

$$d^* = \sqrt{3}\boldsymbol{\eta} : [(1-\theta)\boldsymbol{u}^\eta + \frac{\theta}{2}(\boldsymbol{u}^\eta + \boldsymbol{u}^s)] \tag{B.18}$$

Plugging equation (B.17) into equation (B.18) we get a quadratic equation that can be solved for d^* as follows

$$\frac{2}{\sqrt{3}}(d^*)^2 - (\boldsymbol{\eta} : \boldsymbol{u}^s + \|\boldsymbol{\eta}\|)d^* + 3\gamma_n(\boldsymbol{\eta} : \boldsymbol{u}^s - \|\boldsymbol{\eta}\|) = 0 \tag{B.19}$$

The real positive root of the above quadratic equation is taken as the estimate for d. The value of $\Delta\gamma$ can now be calculated using equations (B.13) and (B.15). A semi-implicit estimate of the deviatoric stress can be obtained at this stage by integrating equation (B.7)$_2$

$$\tilde{\boldsymbol{s}}_{n+1} = \boldsymbol{s}_n + 2\mu\left(\eta\Delta t - \sqrt{3}\Delta\gamma\frac{\tilde{\boldsymbol{s}}_{n+1}}{\|\boldsymbol{s}_{n+1}\|}\right) \tag{B.20}$$

$$= \boldsymbol{s}_n + 2\mu\left(\eta\Delta t - \frac{3}{\sqrt{2}}\Delta\gamma\frac{\tilde{\boldsymbol{s}}_{n+1}}{\sigma_y}\right) \tag{B.21}$$

Solving for $\tilde{\boldsymbol{s}}_{n+1}$, we get

$$\tilde{\boldsymbol{s}}_{n+1} = \frac{\boldsymbol{s}_{n+1}^{\text{trial}}}{1 + 3\sqrt{2}\mu\dfrac{\Delta\gamma}{\sigma_y}} \tag{B.22}$$

where $\boldsymbol{s}^{\text{trial}}_{n+1} = \boldsymbol{s}_n + 2\mu\Delta t\boldsymbol{\eta}$. A final radial return adjustment is used to move the stress to the yield surface

$$\boldsymbol{s}_{n+1} = \sqrt{\frac{2}{3}}\sigma_y \frac{\tilde{\boldsymbol{s}}_{n+1}}{\|\tilde{\boldsymbol{s}}_{n+1}\|} \tag{B.23}$$

A pathological situation arises if $\gamma_n = \boldsymbol{u}_n : \boldsymbol{\eta}_n$ is less than or equal to zero or $\Delta\gamma_{\text{er}} \geq \frac{d^*}{3}\Delta t$. This can occur is the rate of plastic deformation is small compared to the rate of elastic deformation or if the timestep size is too small (see Nemat-Nasser and Chung (1992)). In such situations, we use a locally implicit stress update that uses Newton iterations (as discussed in Simo and Hughes (1998), page 124) to compute $\tilde{\boldsymbol{s}}$.

C Computation of Metrics

The length of the elastic zone after deformation (X_f) is determined by checking the deformed diameter with the original diameter of the cylinder. If the difference is greater than 0.003 mm, plastic deformation is assumed to have taken place. The value of X_f is the distance from the free end of the cylinder to the first point from the free end where the above criterion is met.

Let the closed polygon representing the final profile of the Taylor cylinder be given by $P = p_1, p_2, p_3, ..., p_n, p_{n+1} = p_1$, where n is the number of vertices of the polygon. We assume that the points are ordered in the counter-clockwise direction. Each point p_i has a pair of coordinates (x_i, y_i).

Then, the area of the profile (A_f) is given by

$$A_f = \frac{1}{2}\sum_{i=1}^{n}(x_i\, y_{i+1} - x_{i+1}\, y_i)\ . \tag{C.1}$$

The centroid of the profile is given by

$$C_{xf} = \frac{1}{6A_f}\sum_{i=1}^{n}(x_i\, y_{i+1} - x_{i+1}\, y_i)(x_i + x_{i+1}) \tag{C.2}$$

$$C_{yf} = \frac{1}{6A_f}\sum_{i=1}^{n}(x_i\, y_{i+1} - x_{i+1}\, y_i)(y_i + y_{i+1})\ . \tag{C.3}$$

The volume of the deformed cylinder is given by the Pappus theorem. The formula for the volume is

$$V_f = 2\pi C_{xf} A_f\ . \tag{C.4}$$

The moments of inertia are computed by converting the volume integral into a surface integral over the boundary of the profile. The resulting formulas for the moments of inertia are

$$I_{xf} = -\frac{1}{12}\sum_{i=1}^{n}(x_{i+1} - x_i)(y_{i+1} + y_i)(y_{i+1}^2 + y_i^2) \tag{C.5}$$

$$I_{yf} = \frac{1}{12}\sum_{i=1}^{n}(y_{i+1} - y_i)(x_{i+1} + x_i)(x_{i+1}^2 + x_i^2)\ . \tag{C.6}$$

REFERENCES

Abed, F. H., Voyiadjis, G. Z., 2005. A consistent modified Zerilli-Armstrong flow stress model for bcc and fcc metals for elevated temperatures. Acta Mechanica 175, 1–18.

Babuska, I., Oden, J. T., 2004. Verification and validation in computational engineering and science: basic concepts. Comput. Methods Appl. Mech. Engrg. 193, 4057–4066.

Banerjee, B., 2004a. MPM validation: Sphere-cylinder impact: Low resolution simulations. Tech. Rep. C-SAFE-CD-IR-04-002, Center for the Simulation of Accidental Fires and Explosions, University of Utah, USA. http://www.csafe.utah.edu/documents/C-SAFE-CD-IR-04-002.pdf

Banerjee, B., 2004b. MPM validation: Sphere-cylinder impact: Medium resolution simulations. Tech. Rep. C-SAFE-CD-IR-04-003, Center for the Simulation of Accidental Fires and Explosions, University of Utah, USA. http://www.csafe.utah.edu/documents/C-SAFE-CD-IR-04-003.pdf

Banerjee, B., 2004c. MPM validation: Sphere-cylinder impact tests: Energy balance. Tech. Rep. C-SAFE-CD-IR-04-001, Center for the Simulation of Accidental Fires and Explosions, University of Utah, USA. http://www.csafe.utah.edu/documents/C-SAFE-CD-IR-04-001.pdf

Banerjee, B., 2005a. The Mechanical Threshold Stress model for various tempers of 4340 steel. arXiv:cond-mat 0510330, 1–39.

Banerjee, B., 2005b. Taylor impact tests: Detailed report. Tech. Rep. C-SAFE-CD-IR-05-001, Center for the Simulation of Accidental Fires and Explosions, University of Utah, USA. http://www.csafe.utah.edu/documents/C-SAFE-CD-IR-05-001.pdf

Banerjee, B., 2005c. Validation of UINTAH: Taylor impact and plasticity models. In: Proc. 2005 Joint ASME/ASCE/SES Conference on Mechanics and Materials (McMat 2005). Baton Rouge, LA.

Bardenhagen, S. G., Guilkey, J. E., Roessig, K. M., BrackBill, J. U., Witzel, W. M., Foster, J. C., 2001. An improved contact algorithm for the material point method and application to stress propagation in granular material. Computer Methods in the Engineering Sciences 2 (4), 509–522.

Bardenhagen, S. G., Kober, E. M., 2004. The generalized interpolation material point method. Comp. Model. Eng. Sci. 5 (6), 477–496.

Burakovsky, L., Preston, D. L., 2000. Analysis of dislocation mechanism for melting of elements. Solid State Comm. 115, 341–345.

Burakovsky, L., Preston, D. L., Silbar, R. R., 2000a. Analysis of dislocation mechanism for melting of elements: pressure dependence. J. Appl. Phys. 88 (11), 6294–6301.

Burakovsky, L., Preston, D. L., Silbar, R. R., 2000b. Melting as a dislocation-mediated phase transition. Phys. Rev. B 61 (22), 15011–15018.

Chen, S. R., Gray, G. T., 1996. Constitutive behavior of tantalum and tantalum-tungsten alloys. Metall. Mater. Trans. A 27A, 2994–3006.

de St. Germain, J. D., McCorquodale, J., Parker, S. G., Johnson, C. R., Nov 2000. Uintah: a massively parallel problem solving environment. In: Ninth IEEE International Symposium on High Performance and Distributed Computing. IEEE, Piscataway, NJ, pp. 33–41.

Dobrosavljevic, A. S., Maglic, K. D., 1991. Heat capacity and electrical resistivity of copper research material for calorimetry. High Temperatures-High Pressures 23, 129–133.

Follansbee, P. S., Kocks, U. F., 1988. A constitutive description of the deformation of copper based on the use of the mechanical threshold stress as an internal state variable. Acta Metall. 36, 82–93.

Goto, D. M., Bingert, J. F., Chen, S. R., Gray, G. T., Garrett, R. K., 2000a. The mechanical threshold stress constitutive-strength model description of HY-100 steel. Metallurgical and Materials Transactions A 31A, 1985–1996.

Goto, D. M., Bingert, J. F., Reed, W. R., Garrett, R. K., 2000b. Anisotropy-corrected MTS constitutive strength modeling in HY-100 steel. Scripta Mater. 42, 1125–1131.

Guilkey, J. E., Weiss, J. A., 2003. Implicit time integration for the material point method: Quantitative and algorithmic comparisons with the finite element method. Int. J. Numer. Meth. Engng. 57 (9), 1323–1338.

Guinan, M. W., Steinberg, D. J., 1974. Pressure and temperature derivatives of the isotropic polycrystalline shear modulus for 65 elements. J. Phys. Chem. Solids 35, 1501–1512.

Gust, W. H., 1982. High impact deformation of metal cylinders at elevated temperatures. J. Appl. Phys. 53 (5), 3566–3575.

Hobart, R., 1965. Peierls stress dependence on dislocation width. J. Appl. Phys. 36 (4), 1944–1948.

Hoge, K. G., Mukherjee, A. K., 1977. The temperature and strain rate dependence of the flow stress of tantalum. J. Mater. Sci. 12, 1666–1672.

House, J. W., Lewis, J. C., Gillis, P. P., Wilson, L. L., 1995. Estimation of the flow stress under high rate plastic deformation. Int. J. Impact Engng. 16 (2), 189–200.

Johnson, G. R., Cook, W. H., 1983. A constitutive model and data for metals subjected to large strains, high strain rates and high temperatures. In: Proc. 7th International Symposium on Ballistics. pp. 541–547.

Johnson, G. R., Cook, W. H., 1985. Fracture characteristics of three metals subjected to various strains, strain rates, temperatures and pressures. Int. J. Eng.

Fract. Mech. 21, 31–48.

Johnson, G. R., Holmquist, T. J., 1988. Evaluation of cylinder-impact test data for constitutive models. J. Appl. Phys. 64 (8), 3901–3910.

Jones, S. E., Gillis, P. P., 1987. On the equation of motion of the undeformed section of a Taylor impact specimen. J. Appl. Phys. 61 (2), 499–502.

Kocks, U. F., 2001. Realistic constitutive relations for metal plasticity. Materials Science and Engrg. A317, 181–187.

MacDonald, R. A., MacDonald, W. M., 1981. Thermodynamic properties of fcc metals at high temperatures. Physical Review B 24 (4), 1715–1724.

Marsh, S. P., 1980. LASL Shock Hugoniot Data: Los Alamos series on dynamic material properties. University of California, Berkeley, CA.

Maudlin, P. J., Schiferl, S. K., 1996. Computational anisotropic plasticity for high-rate forming applications. Comput. Methods Appl. Mech. Engrg. 131, 1–30.

McQueen, R. G., Marsh, S. P., Taylor, J. W., Fritz, J. N., Carter, W. J., 1970. The equation of state of solids from shock wave studies. In: Kinslow, R. (Ed.), High Velocity Impact Phenomena. Academic Press, New York, pp. 294–417.

Mitchell, A. C., Nellis, W. J., 1981. Shock compression of aluminum, copper, and tantalum. J. Appl. Phys. 52 (5), 3363–3374.

Nadal, M.-H., Le Poac, P., 2003. Continuous model for the shear modulus as a function of pressure and temperature up to the melting point: analysis and ultrasonic validation. J. Appl. Phys. 93 (5), 2472–2480.

Nemat-Nasser, S., 1991. Rate-independent finite-deformation elastoplasticity: a new explicit constitutive algorithm. Mech. Mater. 11, 235–249.

Nemat-Nasser, S., 2004. Plasticity: A Treatise on Finite Deformation of Heteogeneous Inelastic Materials. Cambridge University Press, Cambridge.

Nemat-Nasser, S., Chung, D. T., 1992. An explicit constitutive algorithm for large-strain, large-strain-rate elastic-viscoplasticity. Comput. Meth. Appl. Mech. Engrg 95 (2), 205–219.

Oberkampf, W. L., Trucano, T. G., Hirsch, C., 2002. Verification, validation, and predictive capability in computational engineering and physics. In: Verfification and Validation for Modeling and Simulation in Computational Science and Engineering Applications. Foundations for Verfification and Validation in the 21st Century Workshop, Johns Hopkins University, Laurel, Maryland.

Osborne, D. W., Kirby, R. K., 1977. Research material 5, copper heat capacity specimen. Tech. Rep. Report of Investigation, National Bureau of Standards, Gaithersburg, MD.

Overton, W. C., Gaffney, J., 1955. Temperature variation of the elastic constants of cubic elements. I. Copper. Physical Review 98 (4), 969–977.

Preston, D. L., Tonks, D. L., Wallace, D. C., 2003. Model of plastic deformation for extreme loading conditions. J. Appl. Phys. 93 (1), 211–220.

Puchi-Cabrera, E. S., Villabos-Gutiérres, C., Castro-Fariñas, G., April 2001. On the mechanical threshold stress of aluminum: Effect of the alloying content. ASME J. Engg. Mater. Tech. 123, 155–161.

Ravichandran, G., Rosakis, A. J., Hodowany, J., Rosakis, P., 2001. On the conversion of plastic work into heat during high-strain-rate deformation. In: Proc. , 12th APS Topical Conference on Shock Compression of Condensed Matter. American Physical Society, pp. 557–562.

Samanta, S. K., 1971. Dynamic deformation of aluminium and copper at elevated temperatures. J. Mech. Phys. Solids 19, 117–135.

Simo, J. C., Hughes, T. J. R., 1998. Computational Inelasticity. Springer-Verlag, New York.

Steinberg, D. J., Cochran, S. G., Guinan, M. W., 1980. A constitutive model for metals applicable at high-strain rate. J. Appl. Phys. 51 (3), 1498–1504.

Steinberg, D. J., Lund, C. M., 1989. A constitutive model for strain rates from 10^{-4} to 10^{6} s^{-1}. J. Appl. Phys. 65 (4), 1528–1533.

Sulsky, D., Chen, Z., Schreyer, H. L., 1994. A particle method for history dependent materials. Comput. Methods Appl. Mech. Engrg. 118, 179–196.

Sulsky, D., Zhou, S., Schreyer, H. L., 1995. Application of a particle-in-cell method to solid mechanics. Computer Physics Communications 87, 236–252.

Taylor, G. I., 1948. The use of flat-ended projectiles for determining dynamic yield stress I. Theoretical considerations. Proc. Royal Soc. London A 194 (1038), 289–299.

Taylor, G. I., Quinney, H., 1934. The latent energy remaining in a metal after cold working. Proc. Royal Soc. Lond. A 143 (849), 307–326.

Varshni, Y. P., 1970. Temperature dependence of the elastic constants. Physical Rev. B 2 (10), 3952–3958.

Wang, L. H., Atluri, S. N., 1994. An analysis of an explicit algorithm and the radial return algorithm, and a proposed modification, in finite elasticity. Computational Mechanics 13, 380–389.

Wang, Y., Chen, D., Zhang, X., 2000. Calculated equation of stae of Al, Cu, Ta, Mo, and W to 1000 GPa. Physical Review Letters 84 (15), 3220–3223.

Wilkins, M. L., 1999. Computer Simulation of Dynamic Phenomena. Springer-Verlag, Berlin.

Wilkins, M. L., Guinan, M. W., 1973. Impact of cylinders on a rigid boundary. J. Appl. Phys. 44 (3), 1200–1206.

Zerilli, F. J., 2004. Dislocation mechanics-based constitutive equations. Metall. Mater. Trans. A 35A, 2547–2555.

Zerilli, F. J., Armstrong, R. W., 1987. Dislocation-mechanics-based constitutive relations for material dynamics calculations. J. Appl. Phys. 61 (5), 1816–1825.

Zerilli, F. J., Armstrong, R. W., 1993. Constitutive relations for the plastic deformation of metals. In: High-Pressure Science and Technology - 1993. American Institute of Physics, Colorado Springs, Colorado, pp. 989–992.

Zocher, M. A., Maudlin, P. J., Chen, S. R., Flower-Maudlin, E. C., 2000. An evaluation of several hardening models using Taylor cylinder impact data. In: Proc. , European Congress on Computational Methods in Applied Sciences and Engineering. ECCOMAS, Barcelona, Spain.